Combustion and Flame 000 (2019) 1–19

Contents lists available at ScienceDirect

Combustion and Flame

journal homepage: www.elsevier.com/locate/combustflame

LES of a swirl-stabilized kerosene spray flame with a multi-component vaporization model and detailed chemistry

Georg Eckel*, Jasper Grohmann, Luca Cantu, Nadja Slavinskaya, Trupti Kathrotia, Michael Rachner, Patrick Le Clercq, Wolfgang Meier, Manfred Aigner

German Aerospace Center (DLR), Institute of Combustion Technology Pfaffenwaldring 38–40, 70569 Stuttgart, Germany

ARTICLE INFO

Article history:
Received 30 November 2018
Revised 25 February 2019
Accepted 7 May 2019
Available online xxx

Keywords:
Multi-phase LES
Swirl-stabilized spray flame
Kerosene combustion
Multi-component fuel
Finite-rate chemistry

ABSTRACT

Due to the introduction of alternative aviation fuels, new methods and models are necessary which have the capability to predict the performance of combustors dependent on the fuel composition. Towards this target, a multi-component vaporization model is coupled to a direct, detailed chemistry solver in the context of Eulerian–Lagrangian LES. By means of the computational platform, a lab-scale, swirl-stabilized spray flame is computed. The burner exhibits some of the key features of current aero-engine combustors. Global features like the measured spray distribution and the position of the reaction zone are well reproduced by the LES. The comparison of droplet size, droplet velocity and liquid volume flux profiles with experimental data also show a good agreement. However, discrepancies in the temperature profiles in the central mixing zone exist. The computational results show that evaporation and mixing are the rate-controlling steps in the flame zone. In this zone, chemistry can be assumed to be infinitely fast. However, other zones exist where finite rate chemistry effects prevail. For these states, the direct computation of the elementary reactions by means of Arrhenius equations and the transport of all individual species are beneficial. Furthermore, the finite rate chemistry approach demonstrates a great potential with respect to pollutant formation, as precursors can be directly computed. Additionally, the example of benzene forming from one specific chemical class in the fuel suggests that a multi-component description of the liquid phase and the evaporation process is required to correctly predict soot emissions.

1. Introduction

During the development process of modern combustors, computational fluid dynamics (CFD) is increasingly used to complement existing industrial knowledge, conception rules, and hardware tests. But, as the sub-processes in a combustor, i.e., fuel atomization, vaporization, mixing and chemical reaction, are highly interdependent, complex flow dynamics and combustion responses develop. The prediction of these coupled unsteady phenomena is still a challenge for current computer models. With respect to unsteady flow features and instabilities, the prediction accuracy of simulations was enhanced in the last decades by the transition from modeling the entire spectrum of turbulent scales (RANS/URANS) to resolving parts of it (LES). LES with detailed models for the individual sub-processes show the potential to support the understanding of fundamental combustion phenomena. Recently, new challenges have arisen due to the introduction of petroleum- based, synthetic and biomass-based alternative fuels [1–3]. Since the first jet engines, the design of combustors has relied on experiences with petroleum-based fuels. Therefore, new methods and models are necessary having the capability to predict the performance and emissions of combustors accounting also for fuel composition effects [4]. With this target in mind, the coupling of a multi-component vaporization model with a direct, detailed gas phase chemistry solver is presented in this paper. By means of the in-house developed computational platform, a lab-scale, swirl-stabilized spray burner is simulated. The burner exhibits some of the key features of current aero-engine combustors. This involves a high complexity due to the fact that a multi-component fuel is introduced via a hybrid fuel injector with a complicated atomization pattern into a complex flow with significant heat loss at the confinements. Accurate predictions of such complex systems are very challenging.

Jet fuels are composed of hundreds of species, e.g., Wahl and Kapernaum [5] identified 410 different species in Jet A-1 by

* Corresponding author.
E-mail address: georg.eckel@dlr.de (G. Eckel).

https://doi.org/10.1016/j.combustflame.2019.05.011

means of a gas chromatograph coupled to a mass spectrometer (GC-MS). Several models can be found in the literature which aim at reducing the number of variables and hence the computational expenses [6]. In the so-called surrogate models, the fuel is represented by one or a few surrogate species. In the early days of combustion simulation, researchers tried to incorporate both physical and chemical properties into a single component surrogate, e.g., n-decane ($C_{10}H_{22}$) represented Jet A-1 in the aerospace industry [6]. Instead of using a single n-alkane species, Rachner et al. [7] proposed a single component surrogate exhibiting the average properties of real multi-component Jet A-1 based on an extensive literature study [8]. Numerical results obtained with this single-component surrogate and experimental data were in good agreement concerning global features of evaporation, mixing [7] and combustion [9]. However, using single-component surrogates, the difference in volatility of the various species in real fuel blends cannot be accounted for. Therefore, Edwards and Maurice [10] recommended a multi-component surrogate, which reflects the important chemical classes and the distillation curve. Jet fuels are mainly composed of n-alkanes, iso-alkanes, cyclo-alkanes and aromatics [11]. Ideally, a multi-component surrogate should mimic physical properties (e.g., density, viscosity, surface tension, thermal conductivity), which are important for atomization, dispersion and vaporization, as well as chemical properties (e.g., laminar flame speed, ignition delay time, adiabatic flame temperature and chemical-class composition), which are important for chemical reaction kinetics, i.e., ignition, combustion and pollutant emissions. However, Violi et al. [12] and Kim et al. [13,14] show the difficulties in optimizing a multi-component surrogate with a small amount of surrogate species to match all of the physical and chemical properties of conventional and alternative jet fuels. Tamim and Hallett [15] as well as Hallett [16] proposed an alternative, in which the composition of mixtures with a large number of components is described by means of distribution functions. The number of variables is reduced to a few distribution parameters while the entire spectrum from light to heavier components in the mixture is considered. By means of this model, Le Clercq and Bellan [17,18] performed direct numerical simulations of the evaporation of gasoline, diesel and three types of kerosene (Jet A, RP-1, JP-7) in gaseous mixing layers laden with liquid drops. The results show that the thermo-physical properties and hence vaporization can be accurately described while the computational costs are kept at reasonable levels. Furthermore, the optimization of the multi-component surrogate can exclusively focus on chemical properties. Consequently, the Large Eddy Simulations presented in this paper follow the same modeling approach for vaporization.

The vaporization of complex mixtures also poses challenges to the computation of chemical reactions. Most acceleration techniques for the computation of the chemical reactions rely on look-up tables which consist of solutions for pre-computed laminar flames, e.g., Flamelet Generated Manifolds (FGM). Even in sophisticated versions, which account for the combustion regime [19] and spray evaporation [20], the tabulation is based on a constant fuel composition reacting with the oxidizer. However, the differences in volatility of the individual species in complex fuel mixtures lead to non-constant, time- and space-varying fuel compositions in the gas phase. This is a serious challenge for tabulation techniques. As a consequence, several research groups are working on reaction mechanisms for real fuel chemistry [21–23] and their inclusion into LES codes [24–28]. In the work at hand, the chemical reactions are directly calculated by a finite-rate chemistry (FRC) approach during run-time. In the FRC model, the rate constants are directly determined from the Arrhenius laws based on the local composition. Unfortunately, this comes along with the necessity of solving a transport equation for each species.

In the following Section 2, the computational platform and the underlying equations will be presented in more detail. First of all, Section 2.1 introduces the detailed chemistry solver. Subsequently, the Lagrangian solver for the liquid phase and the coupling of the multi-component vaporization model with the detailed chemistry solver will be explained (Section 2.2). Thereafter, the test case and the numerical setup will be introduced (Section 3) before the results will be reported (Section 4). The paper finishes with the main findings and some concluding remarks (Section 5).

2. Computational platform

After the bulk liquid is atomized, the physical system consists of discrete liquid droplets with a spectrum of diameters being dispersed in a turbulent, continuous gaseous phase. Due to the very large number of droplets, resolving the detailed evolution of the gas-liquid interfaces as well as the flow on both sides of the interfaces will not be feasible in the foreseeable future. Therefore, within this paper, the gaseous phase is calculated by a finite volume solver in the Eulerian reference frame while the liquid phase is computed by means of Lagrangian particle tracking using a point source approximation. In the latter, droplets are assumed to be mathematical points providing point sources and point forces to the gas field. This comes along with shortcomings in the dense spray region. In thermal turbomachinery however, the dense spray region is confined to a small area close to the fuel injector so that a dilute spray prevails in the major part of the combustion chamber [29]. Data are exchanged online between both solvers via an iterative two-way-coupling procedure.

2.1. Gas flow solver

The flow in the gaseous phase is computed by the finite-volume solver THETA. Unstructured dual grids allow for the simulation of flows in and around complex geometries. In combination with a second-order Crank–Nicolson time discretization scheme, a low-dissipation low-dispersion central second-order scheme [30] is used to calculate the convective and diffusive fluxes. The pressure-velocity coupling is based on a projection method. The FGMRES method preconditioned by a single multigrid V-cycle and the BiCGStab method with Jacobi preconditioning are applied to solve the Poisson equation for the pressure correction and the other transport equations, respectively [30].

2.1.1. Gas phase equations

Large Eddy Simulations (LES) depend on a scale separation approach, i.e., large scales are separated from the small ones by a filtering operation. Filtering the conservation equation for mass, momentum, enthalpy and species mass results in:

$$\frac{\partial \bar{\rho}_g}{\partial t} + \frac{\partial}{\partial x_i}(\bar{\rho}_g \tilde{u}_i) = \bar{S}^d_\rho \tag{1}$$

$$\frac{\partial}{\partial t}(\bar{\rho}_g \tilde{u}_i) + \frac{\partial}{\partial x_j}(\bar{\rho}_g \tilde{u}_i \tilde{u}_j) - \frac{\partial}{\partial x_j}\left(\bar{\tau}_{ij} - \bar{\rho}_g\left(\widetilde{u_i u_j} - \tilde{u}_i \tilde{u}_j\right)\right) = -\frac{\partial \bar{p}}{\partial x_i} + \bar{\rho}_g f_i + \bar{S}^d_{\rho u} \tag{2}$$

$$\frac{\partial}{\partial t}(\bar{\rho}_g \tilde{h}) + \frac{\partial}{\partial x_i}(\bar{\rho}_g \tilde{u}_i \tilde{h}) + \frac{\partial}{\partial x_i}\left(\bar{q}_i - \bar{\rho}_g\left(\widetilde{u_i h} - \tilde{u}_i \tilde{h}\right)\right) = \frac{d\bar{p}}{dt} + \bar{\rho}_g f_i \tilde{u}_i + \bar{S}^d_h \tag{3}$$

$$\frac{\partial}{\partial t}(\bar{\rho}_g \tilde{Y}_\alpha) + \frac{\partial}{\partial x_i}(\bar{\rho}_g \tilde{u}_i \tilde{Y}_\alpha) + \frac{\partial}{\partial x_i}\left(\bar{j}_{\alpha i} - \bar{\rho}_g\left(\widetilde{u_i Y_\alpha} - \tilde{u}_i \tilde{Y}_\alpha\right)\right) = \bar{S}_{Y_\alpha} + \bar{S}^d_{Y_\alpha} \tag{4}$$

with the filtered source terms $\bar{S}^d_\rho$, $\bar{S}^d_{\rho u}$, $\bar{S}^d_h$, and $\bar{S}^d_{Y_\alpha}$ due to the presence of the liquid droplets. The specific enthalpy of a gas mixture h is defined as:

$$h = \sum_{\alpha=1}^{N_{sp}} h_\alpha Y_\alpha \qquad \text{with} \qquad h_\alpha = \Delta h^0_{f,\alpha} + \int_{T_0}^{T} c_{p,\alpha} dT \tag{5}$$

In Eq. (5), $h^0_{f,\alpha}$ and $c_{p,\alpha}$ represent the heat of formation and the specific isobaric heat capacity of species α, respectively. Within this study, it is assumed that only thermal conduction (Fourier's law) and energy fluxes due to species diffusion contribute to the filtered energy flux $\bar{q}_i$ in Eq. (3), while radiation is neglected. The WALE (Wall-Adapting Local Eddy-viscosity) model [31,32] is applied to determine the unresolved sub-grid Reynolds stresses $\bar{\rho}_g\left(\widetilde{u_i u}_j - \tilde{u}_i\tilde{u}_j\right)$. The unresolved scalar fluxes $\bar{\rho}_g\left(\widetilde{u_i\phi} - \tilde{u}_i\tilde{\phi}\right)$ with $\phi = h, Y_1, \ldots, Y_{sp-1}$ are calculated by means of the widely-used gradient diffusion hypothesis in analogy to the resolved scalar fluxes, i.e. the main scalar gradient drives the scalar transport. A formulation based on Fick's law approximates the filtered species diffusion fluxes $\bar{j}_{\alpha i}$. Differential diffusion was neglected, i.e., it was assumed that $Le = 1$.

2.1.2. Chemical reactions

The conversion of a reactant $\mathcal{M}_\alpha$ into a product by a reaction r is described by [33]:

$$\sum_{\alpha}^{N_{sp}} \nu'_{\alpha,r}\mathcal{M}_\alpha \underset{k_{b,r}}{\overset{k_{f,r}}{\rightleftharpoons}} \sum_{\alpha}^{N_{sp}} \nu''_{\alpha,r}\mathcal{M}_\alpha \tag{6}$$

$\nu'_{\alpha,r}$ and $\nu''_{\alpha,r}$ represent the stoichiometric coefficient of species α on the reactant side and the product side, respectively. The modified Arrhenius equation determines the forward and backward reaction rate $k_{f,r}$ and $k_{b,r}$ [33]:

$$k_r = A_r T^{b_r} exp\left(-\frac{E_{a,r}}{\mathcal{R}T}\right) \tag{7}$$

In the pre-exponential factor, A_r and b_r are a constant and the temperature exponent, respectively. $E_{a,r}$ represents the activation energy of the reaction r. By summing over all reactions in the chemical reaction mechanism and introducing the concentration $[\mathcal{M}_\alpha]$ of species $\mathcal{M}_\alpha$, the unfiltered source term on the right hand side of the equation for mass conservation of species $\alpha = 1, \ldots, N_{sp} - 1$ can be calculated [33]:

$$S_\alpha = M_\alpha \sum_{r=1}^{N_r} \left(\left(\nu''_{\alpha,r} - \nu'_{\alpha,r}\right) \left(k_f \prod_{\beta=1}^{N_{sp}-1} [\mathcal{M}_\alpha]^{\nu'_{\beta,r}} - k_b \prod_{\beta=1}^{N_{sp}-1} [\mathcal{M}_\alpha]^{\nu''_{\beta,r}} \right) \right) \tag{8}$$

The finite-rate chemistry model (FRC) used within this work relies on a direct computation of these terms. This requires solving additional transport equations for all species in the chemical reaction mechanism except for the last one, which is given by $\sum_{\alpha=1}^{N_{sp}} Y_\alpha = 1$. The ideal gas law for a gaseous mixture is used to determine the gas density ρ_g:

$$\rho_g = \frac{p_g}{\mathcal{R}T_g \sum_{\alpha=1}^{N_{sp}} (Y_\alpha / M_\alpha)} \tag{9}$$

To account for the unresolved turbulent fluctuations in the sub-grid scale, an assumed probability density function approach is used to compute the filtered chemical source term $\bar{S}_\alpha$. Therefore, two additional transport equation for the sub-grid scale temperature variance and the sum of the sub-grid scale species variances are solved, assuming that the temperature and the species follow a clipped Gaussian PDF and a multivariate β-PDF, respectively [34]. In total, the entire set comprises $N_{sp} + 6$ transport equations which are directly solved. The chemical surrogate for the vaporized fuel consists of four species, i.e., one representative species for each of the most important chemical classes. N-dodecane ($C_{12}H_{26}$), iso-octane (C_8H_{18}), cyclo-hexane (C_6H_{12}) and toluene (C_7H_8) represent the n-alkanes, iso-alkanes, cyclo-alkanes and aromatics, respectively. In total, the detailed skeletal chemical reaction mechanism for Jet A-1, used within this paper, involves $N_{sp} = 80$ species and a set of $N_r = 464$ elementary reactions. It is based on the kerosene mechanism of Slavinskaya et al. [35] with additional sub-mechanisms for the formation of thermal *NO* and *OH** from Smith et al. [36] and Kathrotia [37], respectively. The chemistry is solved by a fully implicit scheme which is fully coupled with the fluid motion. The source terms are linearized using an analytic expression of the Jacobian [34].

2.2. Liquid phase solver

The DLR in-house Lagrangian particle tracking code SPRAYSIM solves the coupled ordinary differential equations (ODEs) for the location, velocity, diameter, composition, and temperature of the dispersed liquid phase. It relies on the widely-used point source approximation.

2.2.1. Droplet dispersion

The droplet dispersion is calculated by the following ODEs for the droplet location, velocity and diameter:

$$\frac{d\vec{x}_p}{dt} = \vec{u}_p \tag{10}$$

$$\frac{d\vec{u}_p}{dt} = \frac{3}{4}\frac{c_d}{d_p}\frac{\rho_g}{\rho_l}|\vec{u}_g - \vec{u}_p| \cdot (\vec{u}_g - \vec{u}_p) + \left(1 - \frac{\rho_g}{\rho_l}\right)\vec{g} \tag{11}$$

$$\frac{d(d_p)}{dt} = -\frac{d_p}{3}\frac{1}{\rho_l}\frac{d\rho_l}{dt} - \frac{2}{\rho_l}\frac{\dot{m}_{vap}}{\pi d_p^2} \tag{12}$$

In Eq. (11) only the most important accelerations acting on the particle are considered, i.e., the acceleration due to drag (first term on the RHS) and gravity (second term on the RHS). The indices g and l stand for gas and liquid, respectively. The change in droplet diameter d_p (Eq. (12)) can be inferred from mass conservation. The influence of the unresolved (sub-grid scale) turbulent fluctuations on the droplet dispersion is modeled by an anisotropic variant of the stochastic dispersion model of Bini and Jones [38]. Droplet-droplet interactions are neglected. Relying on the point source approximation, the filtered spray source terms in the gas phase equations (Eq. (1)–(4)) are computed following the approach presented in [39]. Droplet break-up was modeled by the cascade atomization and drop breakup (CAB) model of Tanner [40] in conjunction with the droplet deformation law of Schmehl [41] and drag formulae from Clift and Grace [42].

2.2.2. Vaporization model

The vaporization model used for the study at hand is based on the uniform temperature model of Abramzon and Sirignano [43] in combination with the continuous thermodynamics model (CTM) of Doué [44], which is based on the work of Tamim and Hallett [15,16]. It approximates the large number of species in a complex mixture by a continuous description via distribution functions. The composition of the Jet A-1 burned in the experiment was determined by GCxGC chromatography. According to their molecular structure, the components ranging from C_6 to C_{17} were grouped into four chemical classes (n-alkanes, iso-alkanes, cyclo-alkanes, and aromatics). Figure 1 shows the chemical composition of the fuel as measured by the GCxGC system (bars) and the approximation by the PDFs (lines). The coupling of fuel vapor species to the chemical surrogate in the gas field CFD code is established by

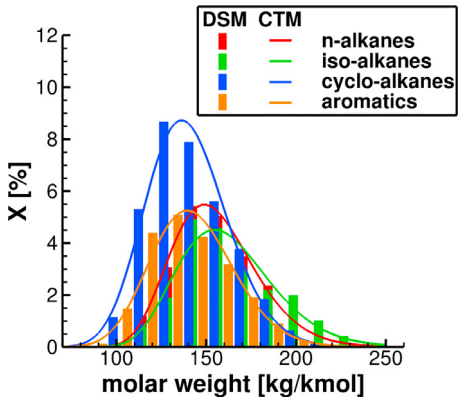

Fig. 1. Discrete species distribution from the GCxGC measurement (bars) and the approximation by the continuous thermodynamics model (lines).

Table 1
Coupling between fuel vapor species and species in the gas phase reaction mechanism.

Fuel vapor species family	Assigned gaseous species in the reaction mechanism
n-alkanes	n-dodecane
Iso-alkanes	Iso-octane
Cyclo-alkanes	Cyclo-hexane
Mono-aromatics	Toluene

assigning one equivalent gaseous species for each family according to Table 1. The continuous thermodynamics model (CTM) can be applied with different distribution parameters, e.g., molar mass, carbon atom number or normal boiling point, depending on accuracy and availability of experimental data. In the following, the concept will be briefly explained based on the molar mass. The total molar mass X_j of a family j results from the sum over the molar masses X_i of species i contained in j:

$$X_j = \sum_{i \in j} X_i \tag{13}$$

Vice versa, the molar mass of an individual species is obtained from the distribution function f_j by:

$$X_i = X_j f_j(I) \Delta I \approx X_j f_j(I) dI \tag{14}$$

The distribution function of each family needs to follow the normalization condition $\int_0^\infty f_j(I) dI = 1$. In the work at hand, each chemical class is represented by a Γ-PDF [45]:

$$f_j(I) = \frac{\left(I - \gamma_j\right)^{\alpha_j - 1}}{\beta_j^{\alpha_j} \Gamma(\alpha_j)} e^{\frac{I-\gamma_j}{\beta_j}} \tag{15}$$

with the origin of the PDF γ_j as well as the parameters α_j and β_j describing the shape of the distribution. $\Gamma(\alpha_j)$ represents the Γ-function given by:

$$\Gamma(\alpha_j) = \int_0^\infty t^{\alpha_j - 1} e^{-t} dt \tag{16}$$

The mean θ_j, the second moment ψ_j and the variance σ_j^2 are related to the distribution parameters α_j, β_j and γ_j by:

$$\begin{aligned} \theta_j &= \alpha_j \beta_j + \gamma_j \\ \sigma_j^2 &= \alpha_j \beta_j^2 \\ \psi_j &= \theta_j^2 + \sigma_j^2 \end{aligned} \tag{17}$$

A drawback of presuming a distribution function is that the basic shape is a priori fixed and cannot change during run-time. Alternatively, the PDF can be described by a Fourier series as shown by Doué [46] and Le Clercq et al. [47] allowing for complexly shaped PDFs. This is especially advantageous in case of condensation. Unfortunately, the description by Fourier series is prone to oscillations tending to under- and overshoot the mole or mass fraction boundaries of [0; 1]. Due to this fact and due to lower computational costs (3–6 Fourier coefficients needed in the Fourier approach), the presumed PDF approach was preferred within the work at hand.

It can be shown [48] that the vaporizing mass flow rate and the change in composition of family j follow the same equations as derived for discrete species [43] replacing the index i for the species by j for the family:

$$\dot{m}_{vap} = \pi d_p Sh \, \rho_g \mathcal{D} \, ln(1 + B_M) \tag{18}$$

with

$$B_M = \frac{Y_j^S - Y_j^\infty}{\zeta_j - Y_j^S} = \frac{\sum_{j=1}^{N_j^S} Y_j^S - \sum_{j=1}^{N_j^\infty} Y_j^\infty}{1 - \sum_{j=1}^{N_j^S} Y_j^S} \tag{19}$$

and

$$\zeta_j = \sum_{i \in j} \zeta_i = \frac{\dot{m}_{j,vap}}{\dot{m}_{vap}} = \frac{Y_j^S (1 + B_M) - Y_j^\infty}{B_M} \tag{20}$$

The change in composition of family j is given by:

$$\frac{dY_{j,l}}{dt} = \frac{6 \dot{m}_{vap}}{\rho_l \pi d_p^3} \left(Y_{j,l} - \zeta_j\right) \tag{21}$$

The species distribution can be computed by means of the mass fractions of the N_j families and the ODEs for the first and second moments given by [48]:

$$\frac{d\theta_{j,l}}{dt} = \frac{6 \dot{m}_{vap}}{\rho_l \pi d_p^3} \frac{\bar{M}_{j,l}}{Y_{j,l} B_M} \left(\frac{Y_{j,g}^\infty \left(\theta_{j,g}^\infty - \theta_{j,l}\right)}{\bar{M}_{j,g}^\infty} - \frac{Y_{j,g}^S \left(\theta_{j,g}^S - \theta_{j,l}\right)}{\bar{M}_{j,g}^S} (1 + B_M) \right) \tag{22}$$

$$\frac{d\psi_{j,l}}{dt} = \frac{6 \dot{m}_{vap}}{\rho_l \pi d_p^3} \frac{\bar{M}_{j,l}}{Y_{j,l} B_M} \left(\frac{Y_{j,g}^\infty \left(\psi_{j,g}^\infty - \psi_{j,l}\right)}{\bar{M}_{j,g}^\infty} - \frac{Y_{j,g}^S \left(\psi_{j,g}^S - \psi_{j,l}\right)}{\bar{M}_{j,g}^S} (1 + B_M) \right) \tag{23}$$

The change in droplet temperature for the mixture yields:

$$\frac{dT_p}{dt} = -\frac{1}{c_{p_l}} \frac{6 \dot{m}_{vap}}{\rho_l \pi d_p^3} \sum_j \left(\Delta \hat{h}_{vap_j} - \frac{\hat{c}_{p_j} \left(T_g^\infty - T_g^S\right)}{B_T} \right) \tag{24}$$

In Eq. (24), the specific heat of evaporation and the specific isobaric heat capacities are replaced by their molar PDF-representation $\Delta h_{vap_i} = \Delta H_{vap_i}(T_l, I_i)/M_j(I_i)$ and $c_{p_i} = C_{p_i}(T_{ref}, I_i)/M_j(I_i)$ and the following abbreviations are brought in:

$$\begin{aligned} \Delta \hat{h}_{vap_j} &= \sum_{i \in j} \left(\frac{X_{j,g}^S f_{j,g}^S(I_i)(1 + B_M)}{\bar{M}_g^S B_M} - \frac{X_{j,g}^\infty f_{j,g}^\infty(I_i)}{\bar{M}_g^\infty B_M} \right) \Delta H_{vap_j}(T_l, I_i) \Delta I_i \\ &\approx \int_{\gamma_j}^\infty \left(\frac{X_{j,g}^S f_{j,g}^S(I)(1 + B_M)}{\bar{M}_g^S B_M} - \frac{X_{j,g}^\infty f_{j,g}^\infty(I)}{\bar{M}_g^\infty B_M} \right) \Delta H_{vap_j}(T_l, I) dI \end{aligned} \tag{25}$$

$$\begin{aligned} \hat{c}_{p_j} &= \sum_{i \in j} \left(\frac{X_{j,g}^S f_{j,g}^S(I_i)(1 + B_M)}{\bar{M}_g^S B_M} - \frac{X_{j,g}^\infty f_{j,g}^\infty(I_i)}{\bar{M}_g^\infty B_M} \right) C_{p_j}(T_{ref}, I_i) \Delta I_i \\ &\approx \int_{\gamma_j}^\infty \left(\frac{X_{j,g}^S f_{j,g}^S(I)(1 + B_M)}{\bar{M}_g^S B_M} - \frac{X_{j,g}^\infty f_{j,g}^\infty(I)}{\bar{M}_g^\infty B_M} \right) C_{p_j}(T_{ref}, I) dI \end{aligned} \tag{26}$$

In the equations derived above, several physical properties are needed in a continuous form. The correlations are taken from Eckel [48].

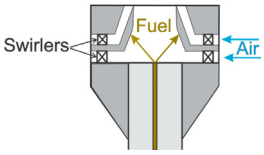

Fig. 2. Sketch of the pre-filming airblast atomizer.

The unresolved (sub-grid scale) turbulent fluctuations around the droplet result in an enhanced mixing and an increase in the heat and mass transfer, which is only partly covered by the sub-grid scale model for droplet dispersion. Therefore, the Nusselt and Sherwood numbers are additionally corrected by empirical correlations from Clift et al. [42, pp. 266–271].

3. Test case description and numerical setup

The generic swirl-stabilized spray burner with a pre-filming airblast atomizer was experimentally investigated by Grohmann et al. [49,50]. The spray was generated by a pre-filming airblast atomizer that is schematically shown in Fig. 2. Air at 323 K was supplied from a plenum to two swirlers that generate co-rotating flows in the inner and outer nozzle vanes. Fuel was sprayed onto the inner surface of the nozzle by a pressure-swirl atomizer (Schlick Mod. 121) which produced a hollow cone spray. The fuel film was transported by the air flow to the atomizer lip where it was re-atomized and injected into the combustion chamber. The diameters of the inner and outer nozzle were 8 and 11.6 mm, respectively. The vertically standing combustion chamber had a cross section of 85×85 mm and a height of 169 mm. Four quartz plates provided optical access to the flame for the application of optical and laser-based measurement techniques. The top plate was equipped with a round exit port (Ø = 40 mm) for the exhaust gas. The cold gas flow field was measured by Particle Image Velocimetry (PIV). Phase Doppler Anemometry (PDA) and a Mie-scattering technique were applied to determine the spray characteristics. The reactive case was qualitatively characterized by CH^*-Chemiluminescence. Furthermore, temperature measurements were performed applying Coherent Anti-Stokes Raman Scattering (CARS) spectroscopy. For this paper, the baseline condition listed in Table 2 was simulated.

Table 2
Boundary conditions of the experiment at baseline conditions.

Fuel	Jet A-1		
Liquid temperature	T_{liq}	$[K]$	303
Fuel mass flow rate	$\dot{m}_{fuel}$	$[g/h]$	850
Oxidizer	Air		
Air pressure	p_{air}	$[bar]$	1.0
Air temperature	T_{air}	$[K]$	323
Air mass flow rate	$\dot{m}_{air}$	$[g/s]$	4.31
Geom. swirl numbers	S_{inner} / S_{outer}	$[-]$	1.17 / 1.22
Global equivalence ratio	ϕ	$[-]$	0.8
Thermal power	$P_{thermal}$	[kW]	10.2

3.1. Discretization

The computational domain shown in Fig. 3 comprises the combustion chamber and the air supply system including both swirlers. Due to its complexity, the geometry is discretized by a fully unstructured tetrahedral mesh. The grid is refined in near wall regions as well as within the swirler vanes, the mixing zone and in the vicinity of the flame. The location of the refinement regions is based on the ratio between turbulent and molecular viscosity determined in non-reacting preliminary investigations.

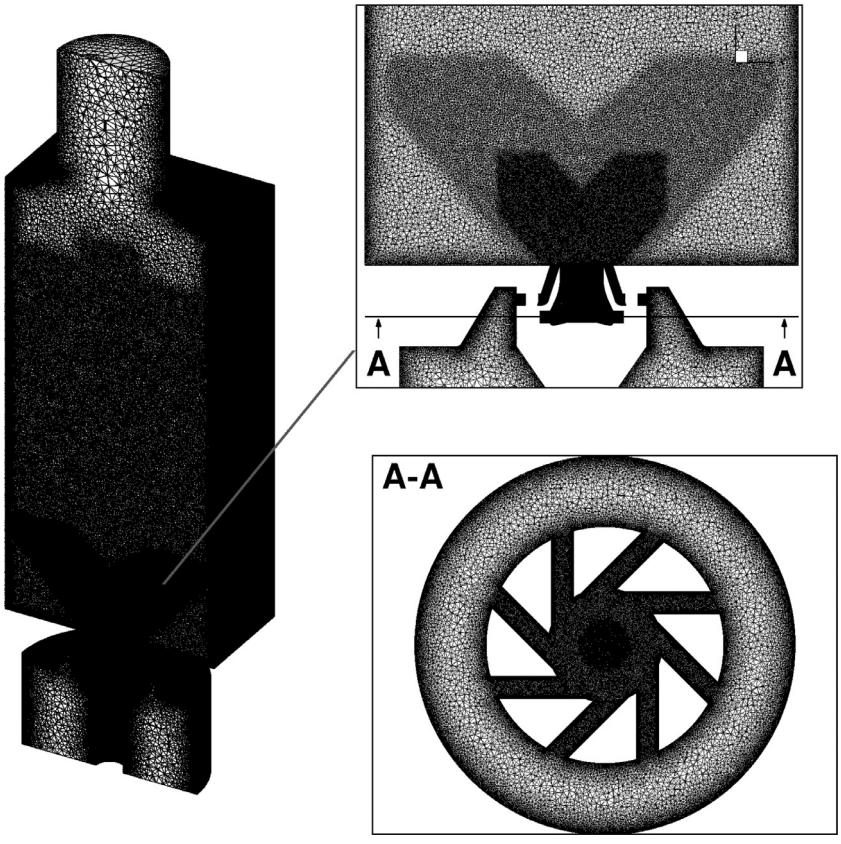

Fig. 3. Computational grid for the swirl-stabilized burner test case.

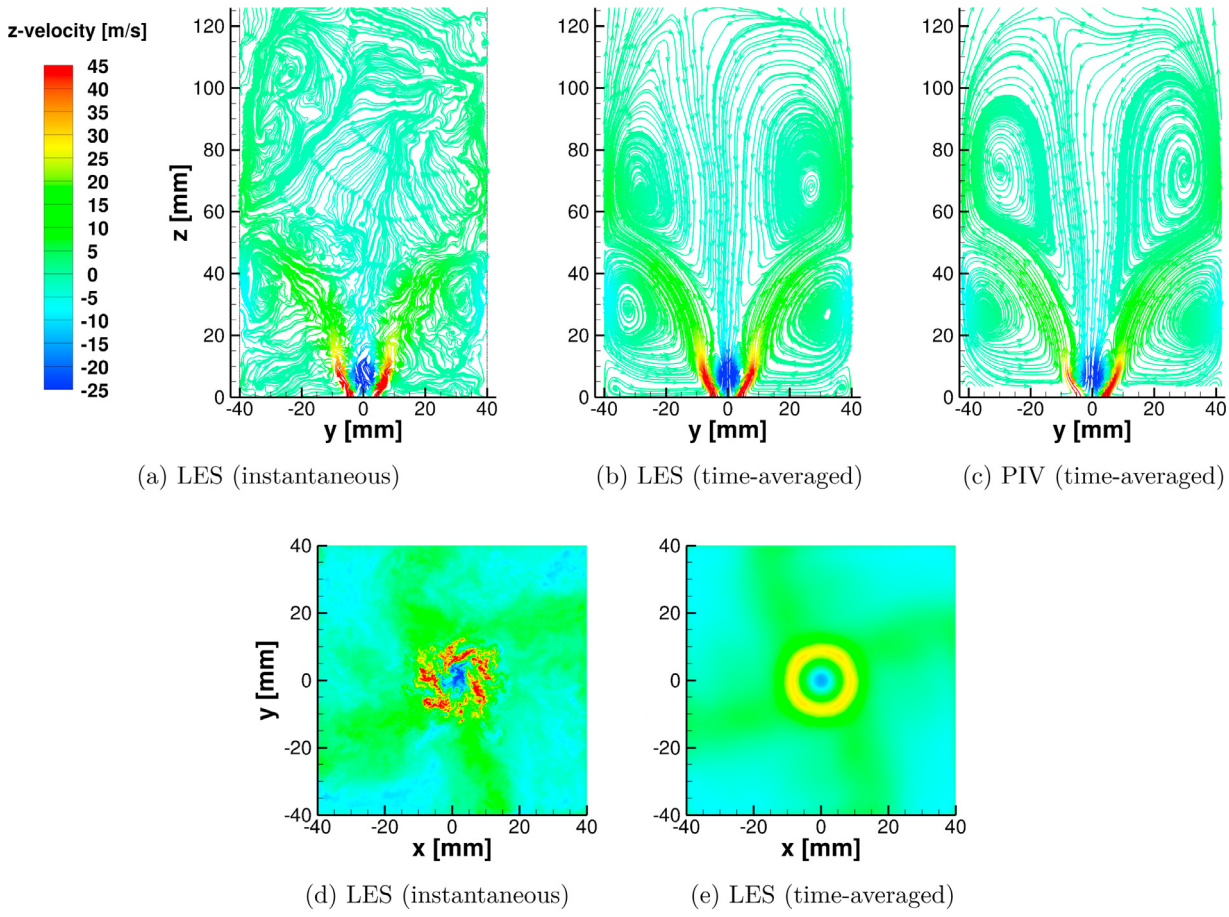

(a) LES (instantaneous) (b) LES (time-averaged) (c) PIV (time-averaged)

(d) LES (instantaneous) (e) LES (time-averaged)

Fig. 4. Instantaneous and time-averaged mean z-velocity field predicted by the LES as well as time-averaged PIV data in the center plane (a-c) and in a horizontal plane at $z = 0.015$ m (d-e) of the non-reacting single phase flow.

This leads to a grid size of 14.7 million points corresponding to 80.7 million tetrahedra.

3.2. Wall boundary conditions

The wall temperatures were experimentally determined by phosphor thermometry [51]. On the bottom plate of the combustion chamber the temperatures are set to a constant value of 717, 901 and 831 K in the central part, the glowing ring and the corners of the bottom plate according to the measured temperatures in these zones, respectively. The side windows are set to a constant temperature of 1205 K being the average temperature of 36 measurement positions (10–120 mm above the burner). All other walls, e.g., within the swirler vanes, the plenum and the outlet, are assumed to be adiabatic.

3.3. Droplet starting conditions

The starting conditions for the droplets are derived from PDA measurements. As measurements close to atomizers are difficult due to the dense spray as well as non-spherical droplets and ligaments [52], the PDA sampling volumes were located 15 mm downstream of the nozzle. However, the simulation requires droplet starting conditions close to the nozzle exit as the heat-up of the spray (e.g., along these 15 mm) strongly influences the position of the reaction zone. Therefore, using the intercept theorem, the measured profiles are projected to an annular area 1.5 mm above the pre-filmer lip with an inner and outer diameter of 7 and 9 mm, respectively. Within this area, the starting positions of the droplets are randomly generated. An automated fitting routine determines the optimum size distribution based on the characteristic diameters for each starting location. This results in a combination of modified log-Rosin-Rammler and root-normal distributions at smaller radii and log-Rosin-Rammler distributions towards larger radii of the annular area. As PDA measurements of the absolute mass flow rate have high uncertainties [52], the local mass flow rate is determined by using the relative information obtained by PDA in conjunction with the total mass flow rate supplied by the mass flow controller.

4. Results

4.1. Flow features of the non-reacting single-phase flow

Figure 4 shows the instantaneous and time-averaged (162.5 ms) flow field of the cold single-phase flow. It can be seen from Fig. 4a that a highly unsteady turbulent flow is present in the combustion chamber. The air exits the nozzle with a high velocity, which induces the generation and shedding of small vortices from the sharp edges. A time-average of the velocity data reveals large (integral scale) flow recirculations (Fig. 4b). A small central recirculation zone forms close to the nozzle exit (-10 mm $< y <$ 10 mm, 0 mm $< z <$ 20 mm). The swirling flow leads to a radial pressure gradient with a low pressure region towards the axis [53]. The expansion after the nozzle causes a decay of the tangential velocity equalizing the radial pressure profile. As a consequence, a negative axial pressure gradient builds up close to the z-axis resulting in a flow reversal. Due to the confinement and driven

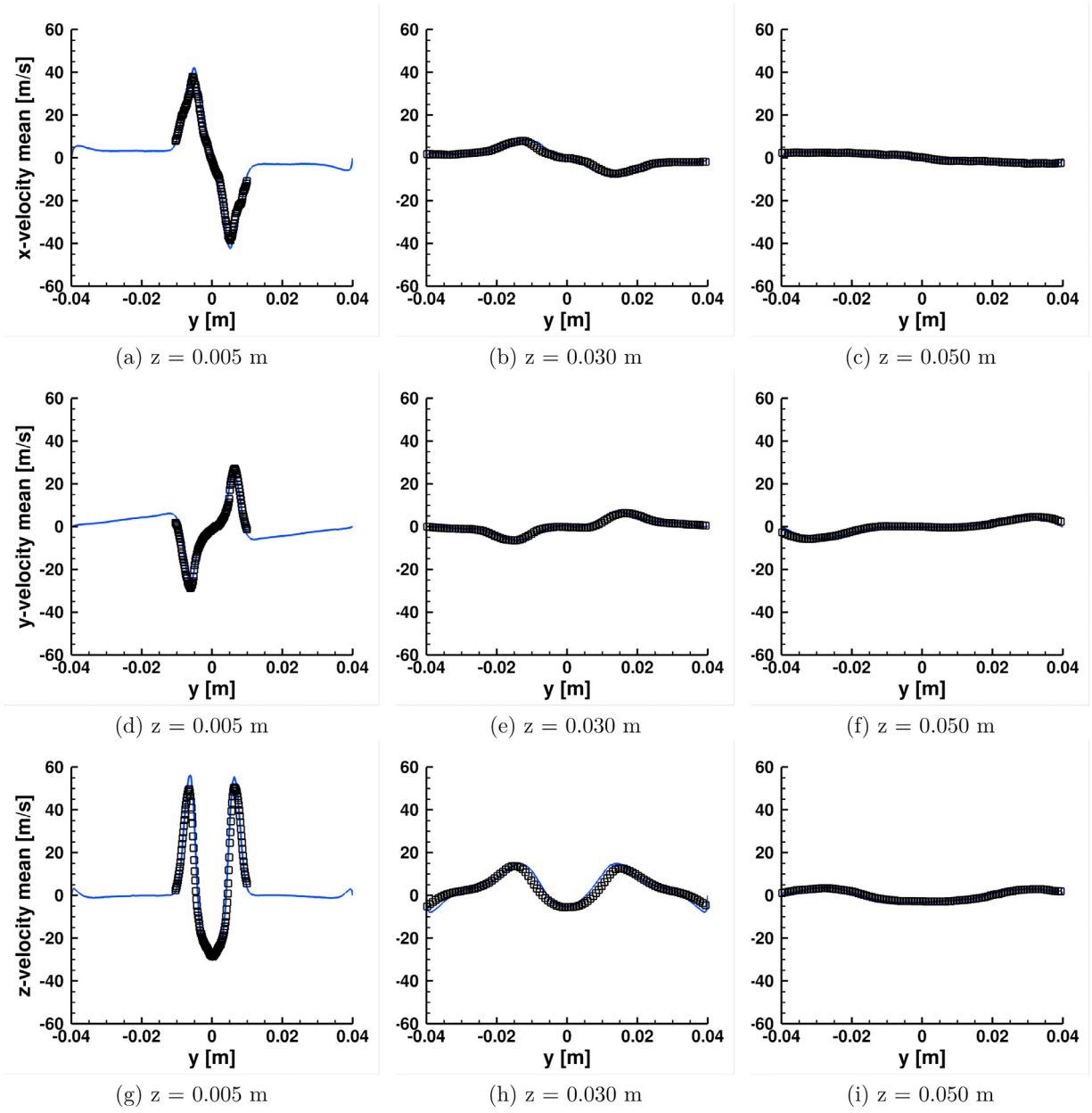

(a) z = 0.005 m (b) z = 0.030 m (c) z = 0.050 m

(d) z = 0.005 m (e) z = 0.030 m (f) z = 0.050 m

(g) z = 0.005 m (h) z = 0.030 m (i) z = 0.050 m

Fig. 5. Time-averaged mean velocity profiles in the center plane at different downstream positions: LES (blue lines) and experimental data (black squares). (For interpretation of the references to color in this figure legend, the reader is referred to the web version of this article.)

by the high momentum air, two pairs of counter-rotating external recirculations establish close to the walls. The low pressure zone close to the central z-axis described before supports the backflow towards the nozzle. Figure 4c depicts experimental data taken by PIV. The agreement of the qualitative flow features between the PIV measurements and the LES prediction in Fig. 4b is excellent. The asymmetry in both the simulated and measured time-averaged flow field is due to the swirl and the change from a circular cross-section of the nozzle to a quadratic cross-section of the vitreous combustion chamber, as can be seen from the z-velocity field in a cross-section 15 mm downstream of the nozzle (Fig. 4d, c).

4.2. Velocity profiles of the non-reacting single-phase flow

To assess the accuracy of the LES computations with respect to the non-reacting single-phase flow, the numerical results are quantitatively compared with the PIV measurements at different downstream positions from the swirler exit plane. The time-averaged mean velocity profiles (x, y, and z-direction) in planes 5–50 mm downstream of the nozzle exit plane are depicted in Fig. 5. The time-averaged velocity fluctuations in the same planes are given in Fig. 6. The blue lines refer to the LES predictions while the black squares represent the experimental PIV data. Except for a slight overshoot in the prediction of the maximum and minimum x- and z-velocity at $z = 0.005$ m, an overall excellent agreement can be observed. The negligible deviations are well within the temporal and spatial accuracy of the measurement system. It is noteworthy that not only the mean quantities but also the fluctuations are remarkably well reproduced.

4.3. Overall characteristics of the reacting multi-phase flow

Figure 7 illustrates the combustion of Jet A-1 in the swirl-stabilized spray burner. The fuel droplets, launched above the

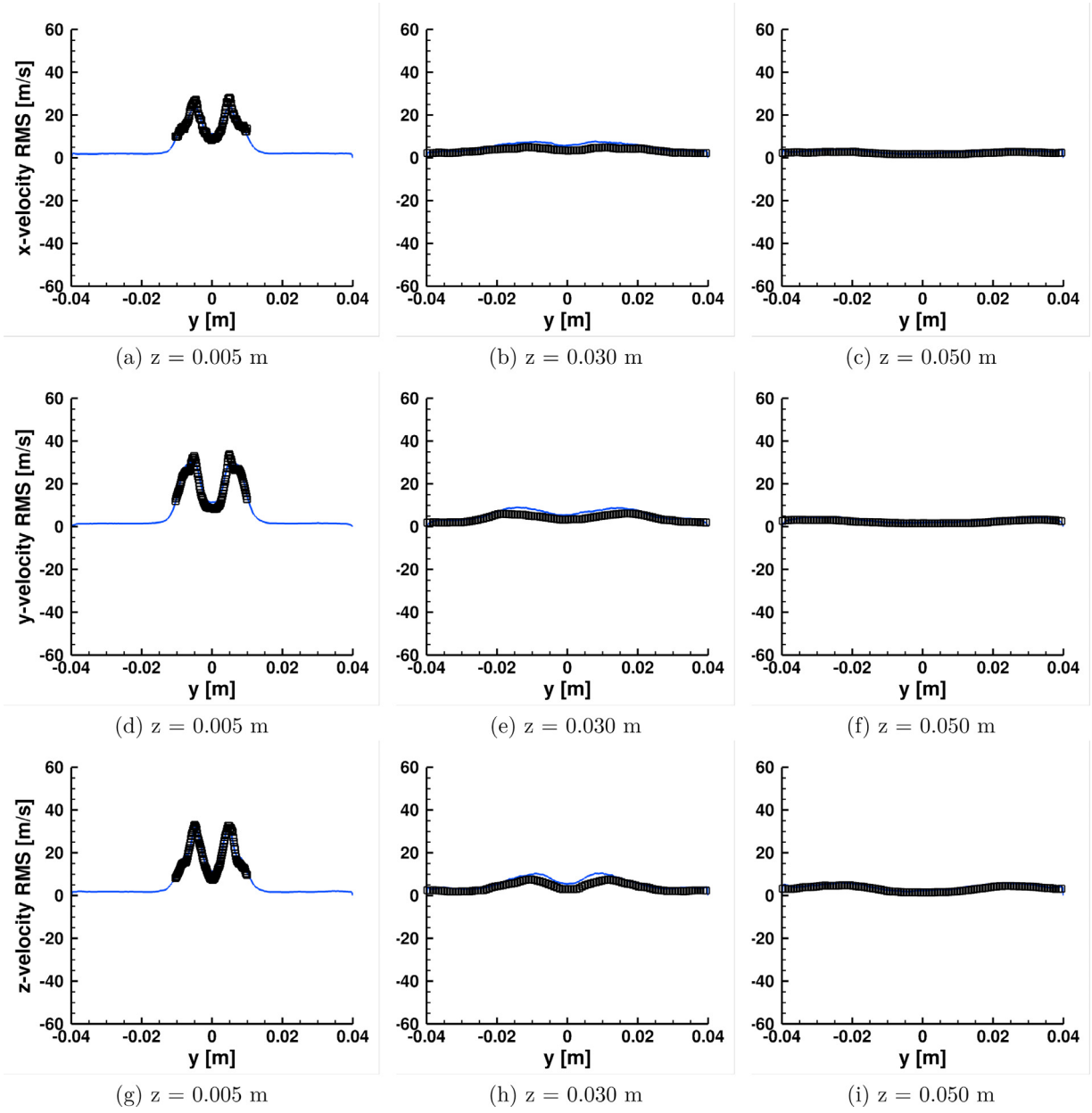

(a) z = 0.005 m (b) z = 0.030 m (c) z = 0.050 m

(d) z = 0.005 m (e) z = 0.030 m (f) z = 0.050 m

(g) z = 0.005 m (h) z = 0.030 m (i) z = 0.050 m

Fig. 6. Time-averaged velocity fluctuations (RMS) profiles in the center plane at different downstream positions: LES (blue lines) and experimental data (black squares). Remark: The RMS values are positive without exception, the profiles were shifted for the sake of visualization. (For interpretation of the references to color in this figure legend, the reader is referred to the web version of this article.)

pre-filmer lip, disperse in the combustion chamber while interacting with the turbulent eddies. During the dispersion, the surrounding hot gases heat up the droplets until they start to evaporate. As soon as the fuel is evaporated, it mixes and reacts with the oxygen in the air. A highly wrinkled flame forms touching the side windows of the combustion chamber.

4.4. Flow and temperature fields of the reacting multi-phase flow

As the air mass flow rate is equivalent to the one in Section 4.1, the reacting multi-phase flow shows strong similarities to the cold single-phase flow. The flow displays a large spectrum of coherent structures and turbulent scales (see Fig. 8). Small vortices are evident in the instantaneous snapshot (Fig. 8a) while the time average (32.5 ms, Fig. 8b) reveals large (integral scale) flow recirculations, which are induced by the swirling high-velocity stream coming from the nozzle. The asymmetry in Fig. 8b is partly due to the swirl and the change from a circular cross-section of the nozzle to a quadratic cross-section of the vitreous combustion chamber (as explained in Section 4.1). However, it is also partly attributed to the fact that the simulation is not yet statistically fully converged in the low speed downstream regions. Due to the immense computational costs of the reacting case, the period for the time-averaging is a factor of 5 shorter than the one in the non-reacting case. The temperature field (Fig. 9) exhibits a high temperature region ($T > 1600\,K$) within the lower external recirculation zones and a low temperature region ($T < 800$ K) in the swirling air stream coming from the nozzle. In the large downstream recirculation zones, the temperature reaches 1400–1500 K. In the central mixing zone, temperatures range from 800 to 1400 K. Furthermore, the cooling (due to the isothermal boundary conditions) in the vicinity of the confinements is visible, i.e., $T \approx 1200$ K close to side windows and $900\ K < T < 1000$ K close to the bottom plate.

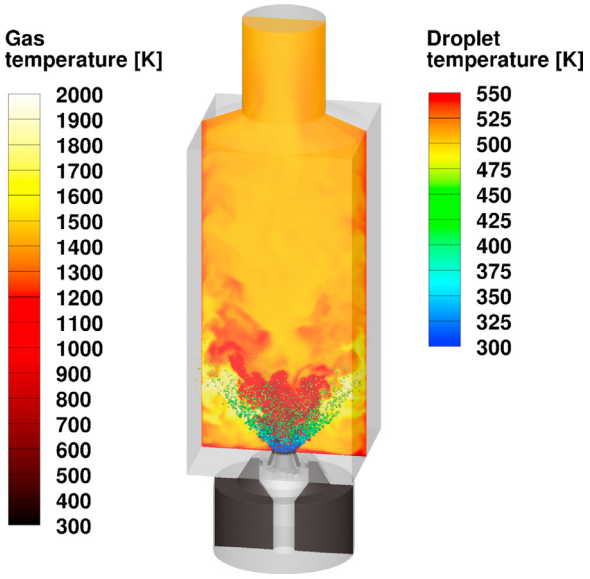

Fig. 7. Spray combustion in the swirl-stabilized spray burner.

A closer look at Fig. 8a reveals a regular flow pattern in the vicinity of the nozzle. As explained in Section 4.1, the swirl (see red spots with high velocities near the nozzle) leads to a static pressure drop close to the central z-axis resulting in a toroidal flow reversal (see vortices in the central recirculation near the nozzle) sucking hot gases back. This so-called precessing vortex core (PVC) is visualized in Fig. 10a. The PVC extends to roughly 2 burner exit diameters from the nozzle exit plane where the vortex starts to break down. The Fourier transformation of the relative pressure signal at a monitor point located within the PVC indicates that the PVC rotates with a frequency of 4180 Hz (see Fig. 10b). Besides the distinct peak at 4180 Hz, a first higher harmonic at 8360 Hz is also visible.

4.5. Droplet distribution and vaporization

Figure 11 shows an instantaneous snapshot of the spray distribution in the center plane of the combustion chamber. On the left, the instantaneous (coloured "speckles") and time-averaged (contour lines) experimental data obtained by evaluating the Mie scattering on the droplets is depicted. On the right, the instantaneous volume faction predicted by the LES is displayed. Although a one to one comparison of instantaneous data is not advisable, Fig. 11 gives an impression of the qualitatively good agreement between simulation and experiment. However, the droplet trajectories in the LES seem to have a slightly steeper angle than the ones observed in the experiment. Besides, the experiments showed that some of the droplets impinge the side windows of the combustion chamber. In the simulation, these droplets undergo a perfectly elastic reflection without any proper droplet-wall interaction model. As only 3.9% of the injected liquid mass hits the side windows in the simulation, an influence is expected to be minor but cannot be excluded. Figure 12 illustrates evaporation related profiles over the axial distance from the nozzle. Each point reflects a registration plane orthogonal to the main flow direction (z-axis). Within the first 0.05 m, the droplets experience the hot combustion zone. The droplet temperature (mass-averaged over each registration plane) rapidly rises from 300 to 450 K (Fig. 12a). In this region, 95 mass-% of the fuel evaporates (Fig. 12b). The mean molar masses of the fuel families rise as the components with shorter chain lengths evaporate more and more (Fig. 12c). At the same time, the PDF distributions become narrower (Fig. 12d). The mass fluxes through the registration planes of the four fuel families (Fig. 12e) indicate that the cyclo-alkanes evaporate first, followed by the iso-alkanes, the n-alkanes and the aromatics. It is explained by looking at the vapor pressure of the four fuel families as a function of temperature (Fig. 12f). The cyclo-alkane family exhibits the highest vapor pressure, followed by the iso-alkane family, the n-alkanes and the aromatics. Here, it should be remarked that the vapor pressure is depicted for an entire family. It depends not only on the physical properties for a specific molecular structure but also on the chain length. For the specific composition of Fig. 1 for example, the cyclo-alkanes hold the molecules with the shortest chain length, i.e., lowest molar mass. This leads to the highest vapor pressure. On the contrary, the lowest vapor pressure is observed for the mono-aromatics, despite the fact that they exhibit similar chain lengths. In this case, the different molecular structures lead to differences in volatility.

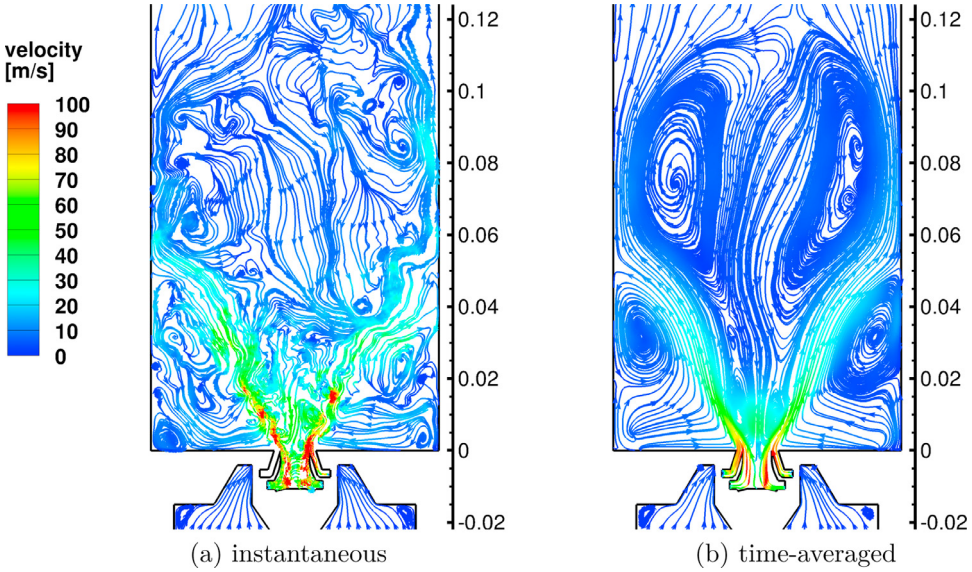

Fig. 8. Calculated streamlines and velocity magnitude in the center plane of the reacting swirl-stabilized spray burner. (For interpretation of the references to color in this figure, the reader is referred to the web version of this article.)

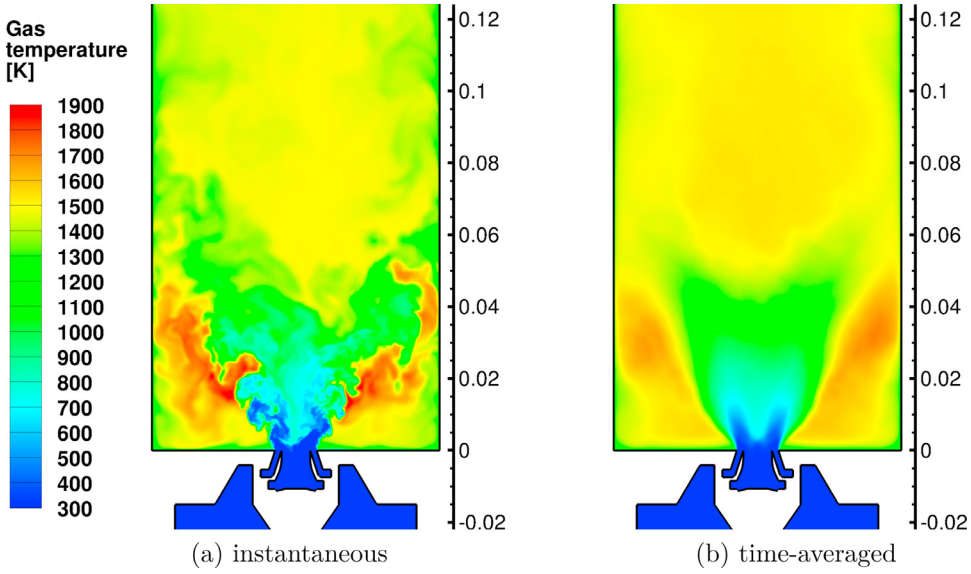

Fig. 9. Calculated temperature field in the center plane of the reacting swirl-stabilized spray burner.

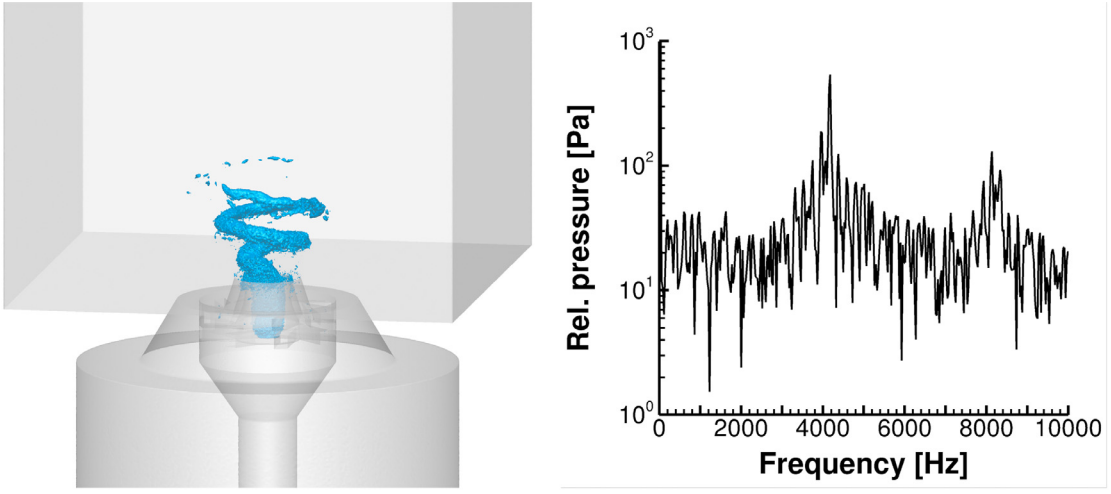

Fig. 10. Precessing vortex core computed by the simulation.

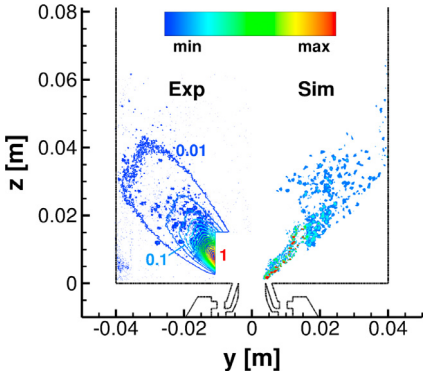

Fig. 11. Experimental (left) and numerical instantaneous spray distribution (right), contour lines represent a time-average of the experimental data.

4.6. Mixing and flame stabilization

Flame stabilization is a central design criterion for combustion chambers in aero-engines as a stable and safe operation has to be guaranteed at any operating point. To understand the flame stabilization in the lab-scale swirl-stabilized spray burner, it it important to analyze, in addition to the vaporization of the fuel components, also the mixing of these components with the oxygen in the air. Therefore, the mixture fraction definition by Bilger et al. [54] is introduced:

$$Z = \frac{2\frac{Y_C}{M_C} + \frac{1}{2}\frac{Y_H}{M_H} + \frac{Y_{O,ox} - Y_O}{M_O}}{2\frac{Y_{C,fuel}}{M_C} + \frac{1}{2}\frac{Y_{H,fuel}}{M_H} + \frac{Y_{O,ox}}{M_O}} \tag{27}$$

It is based on the elemental mass fractions Y_C, Y_H and Y_O of the elements C, H, and O, respectively. Z amounts to $Z = 1$ in the fuel stream (subscript fuel) and $Z = 0$ in the oxidizer stream (subscript

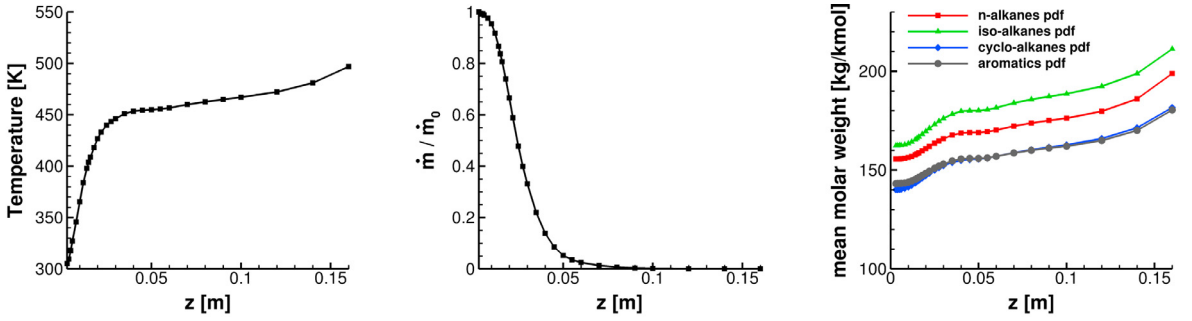

(a) Average droplet temperature (b) Total liquid mass flux normalized by the total injected liquid mass flux (c) Mean molar weight of the Jet A-1 fuel families

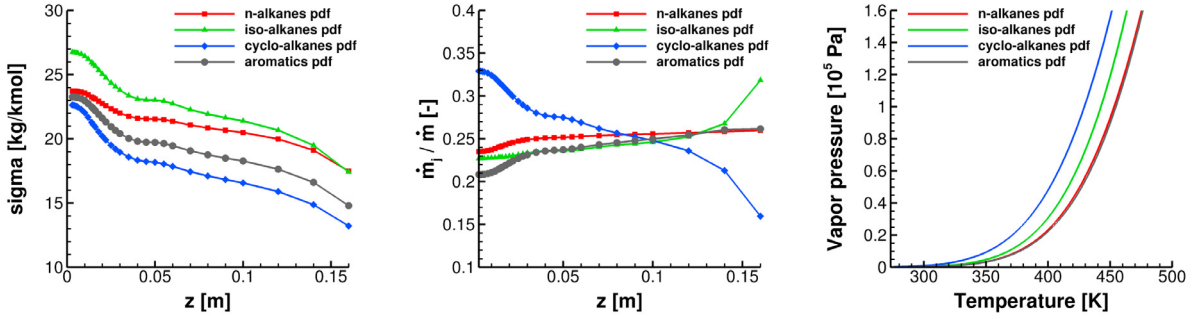

(d) Standard deviation of the molar weight of the Jet A-1 fuel families (e) Mass flux of the Jet A-1 fuel families normalized by the local mass flux (f) Vapor pressure of the Jet A-1 fuel families over temperature

Fig. 12. Evaporation related profiles over the axial distance from the nozzle in the reacting swirl-stabilized spray burner (a–e). Vapor pressure of the individual fuel families for the Jet A-1 composition shown in Fig. 1 as a function of temperature (f).

ox). The stoichiometric value is given by:

$$Z_{st} = \frac{\frac{Y_{O,ox}}{M_O}}{2\frac{Y_{C,fuel}}{M_C} + \frac{1}{2}\frac{Y_{H,fuel}}{M_H} + \frac{Y_{O,ox}}{M_O}} \tag{28}$$

For the investigated condition, the stoichiometric mixture fraction in the swirl-stabilized spray burner yields $Z_{st} = 0.0635$. The mixture fraction Z is a scalar, which varies due to evaporation, diffusion, and convection, not because of reaction or heat extraction. Figure 13 displays the instantaneous temperature field (grey scale contours) in combination with the instantaneous mixture fraction field (lines) as defined by Eq. (27). At a glance, a direct correlation between the both can be noted and different characteristic zones can be identified:

1. Unmixed air stream: The lowest temperatures correspond to a zone close to the nozzle ($T = 323$ K), which is only covered by the oxidizer from the high-velocity swirling air stream (see dark blue lines). In this zone, the droplets have not yet evaporated and no combustion products have yet mixed with the incoming fresh air.
2. Flame zone: The highest temperatures ($T > 1600$ K) are encountered in this region with mixture fractions close to the stoichiometric value of $Z_{st} = 0.0635$ (see green line colors). The majority of the fuel vaporization takes place here and insular spots around droplet clusters with rich mixtures can be found.
3. Lower external mixing zone: This zone is confined by the side windows and the bottom plate of the combustion chamber as well as the flame zone (zone 2) and the unmixed air stream (zone 1). The mixing in this zone is driven by the lower external recirculations. These recirculations transport hot combustion products back towards the burner, where they mix with the incoming fresh air. During this transport, the hot gases are cooled by the side windows and the bottom plate.

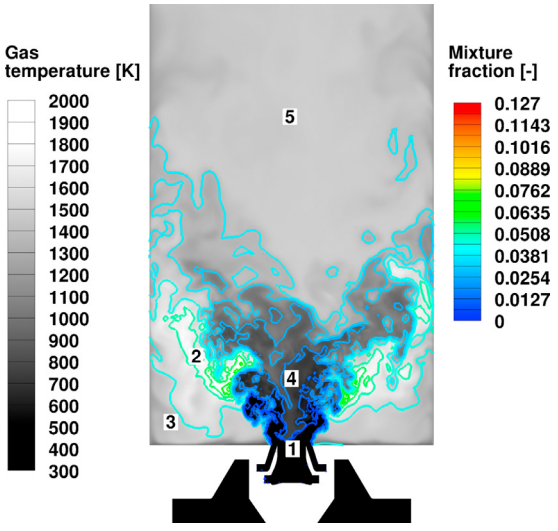

Fig. 13. Instantaneous temperature field (grey scale contour plot) and mixture fraction (colored lines). (For interpretation of the references to color in this figure, the reader is referred to the web version of this article.)

4. Lower central mixing zone: This zone is confined by the unmixed air stream (zone 1) and the upper mixing zone (see below). The mixing in this zone is driven by the small central recirculations and the precessing vortex core, which transport hot gases down to the nozzle exit plane.
5. Upper mixing zone: The mixing in this zone is driven by the upper external recirculations. In the upper external region close to the side windows (especially in the corners of the combustion chamber), hot gases together with unburned droplets from

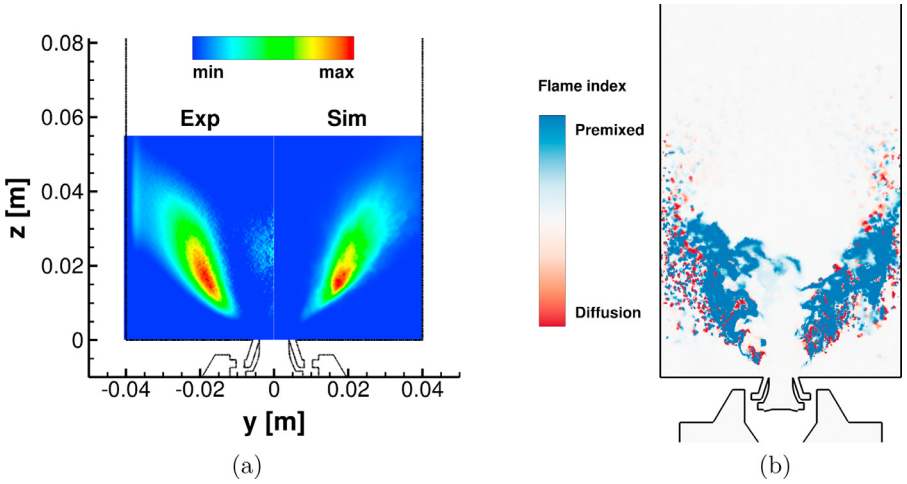

Fig. 14. (a) Time-averaged measured CH*-Chemiluminescence, Abel deconvoluted (left) and time-averaged OH*-distribution predicted by the LES (right); (b) Identification of premixed (blue) and diffusion (red) flame zones by means of the Takeno flame index. (For interpretation of the references to color in this figure legend, the reader is referred to the web version of this article.)

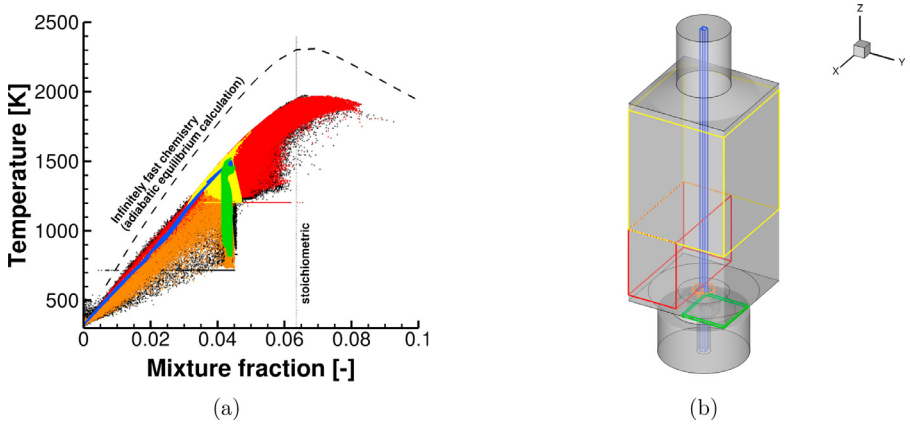

Fig. 15. (a) Scatter plot of the states of the reacting multi-phase flow; (b) Regions corresponding to the colors in the scatter plot. (For interpretation of the references to color in this figure, the reader is referred to the web version of this article.)

the flame zone (zone 2) are entrained into the upper recirculation zone. These hot gases are slightly cooled by the colder side windows and then transported back towards the nozzle in the central region. On their way towards the nozzle, these hot gases mix with the cold flow of the air stream (zone 1).

The recirculation of hot products in the lower external mixing zone (zone 3), the lower central mixing zone (zone 4) and upper mixing zone (zone 5) provides the necessary energy to continuously ignite the incoming reactants after being sufficiently mixed. By the transport of hot combustion products back to the flame root, the flame stabilizes in the lower external recirculation zones along the mean spray trajectory. On a time average basis, a v-shaped flame zone can be observed. Figure 14a illustrates a center plane cut through this flame zone. The LES prediction of the OH*-field (right) is depicted together with the Abel-deconvoluted CH*-Chemiluminescence measured in the experiment (left). Qualitatively, the position of the main flame zone matches well. Although two different chemiluminescent species were used as a marker of the flame zone, Kathrotia et al. [55] and Prabasena et al. [56] showed in one-dimensional flame configurations that both excited species are located very close to each other over a wide range of equivalence ratios. However, they observed two small differences. Firstly, OH* profiles tend to be wider than those of CH*. Secondly, the peak of OH* is slightly shifted towards the lean side, while the CH*-peak appears towards the fuel-rich side. In addition to the effects related to the different chemiluminescent species, the offset might be due to the slightly steeper spray angle of the simulation in comparison to the experimental findings, which was reported in Section 4.5. The discontinuous CH*-Chemiluminescence signal close to the z-axis is an artifact of the Abel transformation. Premixed and diffusion flame zones were identified by means of the Takeno flame index [57]. Figure 14b shows the flame index calculated from the n-dodecane and oxygen mass fraction fields and weighted by the n-dodecane reaction rate [58]:

$$FI = |\dot{\omega}_{nC_{12}H_{26}}| \frac{\nabla Y_{nC_{12}H_{26}} \cdot \nabla Y_{O_2}}{|\nabla Y_{nC_{12}H_{26}} \cdot \nabla Y_{O_2}|} \tag{29}$$

Premixed flames are observed in the inner part of the flame zone, where the highly turbulent flow results in an enhanced mixing. Hence, the scales of the premixed flames are of the order of the turbulent flow structures. Diffusion flames appear on scales of the order of droplet clusters. They are scattered over the entire flame zone with a slightly higher likelihood towards the confinements.

Figure 15a displays the different states of the reacting multi-phase flow system. More precisely, only the gaseous phase is depicted and the temperature is plotted against the mixture fraction (Eq. (27)). Black circles represent all the individual positions in the entire computational domain. Colored data points correspond to the regions in Fig. 15b marked with the same color code. The “frozen chemistry” or “pure mixing” limit is reached if the

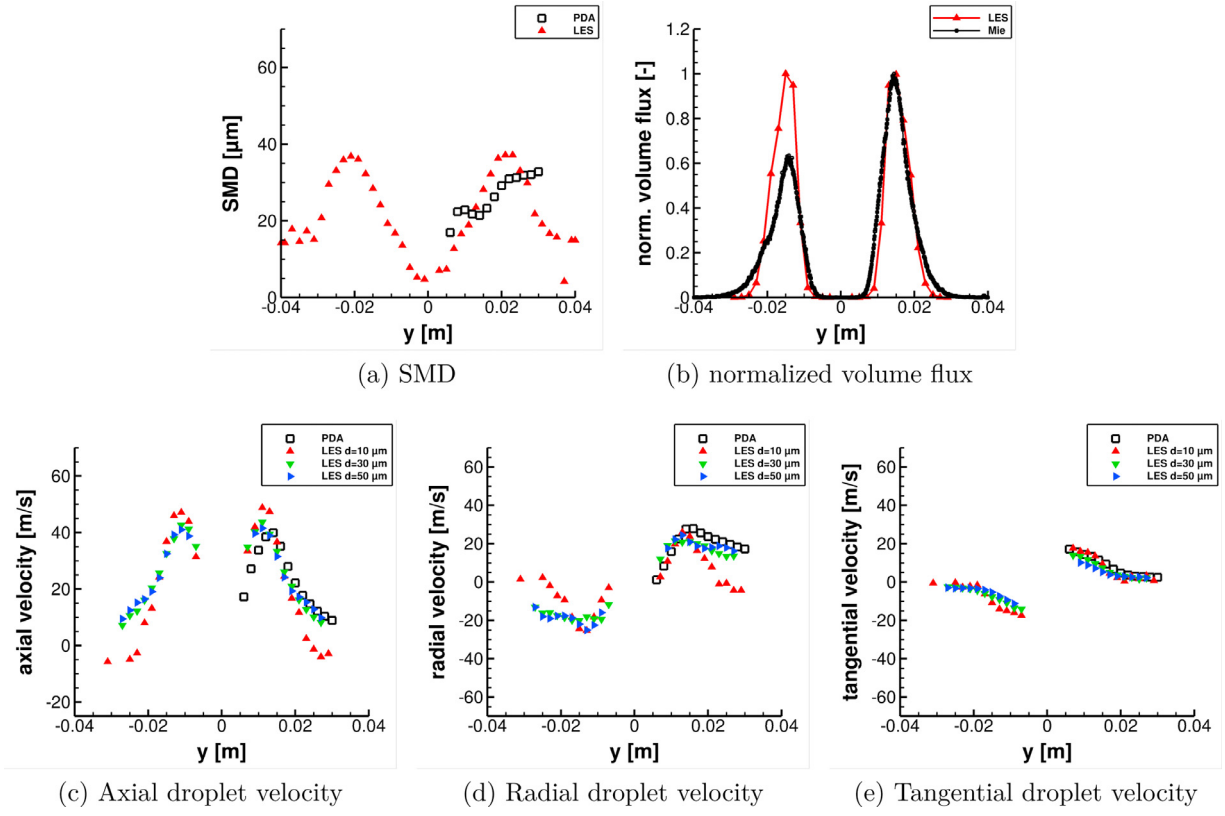

(a) SMD (b) normalized volume flux

(c) Axial droplet velocity (d) Radial droplet velocity (e) Tangential droplet velocity

Fig. 16. Time-averaged profiles of spray characteristics 15 mm downstream of the nozzle: LES (colored symbols) and experimental data (black symbols). (For interpretation of the references to color in this figure, the reader is referred to the web version of this article.)

diffusion and flow time scales are considerably shorter than chemical time scales. In Z-T space, this limit is represented by straight lines. Mixing zones are visible between the flame zone (red) and the side walls with a temperature of 1205 K as well as close to the central axis (blue) and the lower external mixing zone in the vicinity of the injector (orange), where products are transported back towards the nozzle. On the contrary, equilibrium or infinitely fast chemistry is reached if the chemical time scales are considerably shorter than diffusion and flow time scales. The dashed line represents this limit of infinitely fast chemistry under adiabatic conditions determined by an adiabatic equilibrium calculation with CANTERA [59]. The maximum temperature is found around the stoichiometric value of the mixture fraction ($Z = Z_{st} = 0.0635$, dotted line). The dashed limit cannot be reached as the system suffers from heat losses at the side windows and the bottom plate. Therefore, it is concluded that the upper boundary of the scatter points represents the limit of infinitely fast chemistry (equilibrium) under non-adiabatic conditions. A substantial share of the points in the flame zone (red) is located close to this boundary suggesting that these states are controlled by evaporation and mixing and not by the reaction kinetics. However, if all reactions occurred infinitely fast in the entire domain, the *Z-T*-diagram would show distinct curves, i.e., a lower curve representing the unburnt state and an upper curve representing the burnt state. On the contrary, Fig. 15a shows a wide scatter indicating that many states are governed by a finite rate chemistry. In these states, fuel and oxidizer can coexist. Depending on the flow time scales, the evaporation time scales, and the chemical time scales, the situation becomes more complex. The mixtures can be diluted by recirculating reaction products or be influenced by heat transfer in the vicinity of the confinements. For example, the heat loss at the bottom plate (green points/region) leads to a substantial drop in gas temperature, which is limited by the temperatures of the base plate (717, 831 and 901 K, see Section 3.2). However, the temperature drop is not expected to be so pronounced in reality. It is rather a numerical artefact caused by the Dirichlet boundary condition, i.e., due to the assumption of isothermal walls for the bottom plate and the side walls. Furthermore, around droplets and droplet clusters, insular spots of rich mixtures can be found (see points with $Z > 0.0635$).

4.7. Spray characteristics

Figure 16 displays time-averaged profiles of spray characteristics in a plane 15 mm downstream of the nozzle exit. These spray characteristics comprise the Sauter mean diameter (Fig. 16a), the normalized volume flux (Fig. 16b) as well as the axial, radial and tangential droplet velocities (Fig. 16c–e). The LES data is represented by the colored symbols. The experimental data measured by a PDA system is illustrated by black squares. As can be seen from Fig. 16a, the Sauter mean diameter in the LES is in the range $5 - 40\,\mu m$ and shows a distinct peak of $\sim 40\,\mu m$ at $y \approx \pm 0.02$ m. In contrast, the measured SMD almost monotonically increases with the distance from the central axis from $18\,\mu$ to $35\,\mu m$. The discrepancy amounts to 0-8 µm in the region of the maximum volume flux (see Fig. 16 b) and goes up to $12\,\mu m$ for the highest SMD measured. The normalized volume flux (Fig. 16b) predicted by the LES agrees well with the one measured by Mie scattering on the droplets. The asymmetry in the measured profile is due to the fact that the pressure-swirl atomizer located in the center of the airblast atomizer (Fig. 2) produced a non-uniform spray in circumferential direction. This lead to a non-uniform liquid film and hence an asymmetric circumferential spray distribution. This is not accounted for in the simulation. In Fig. 16c–e, the droplet velocities for three diameter classes, i.e., $10\,\mu m$ (red symbols), $30\,\mu m$

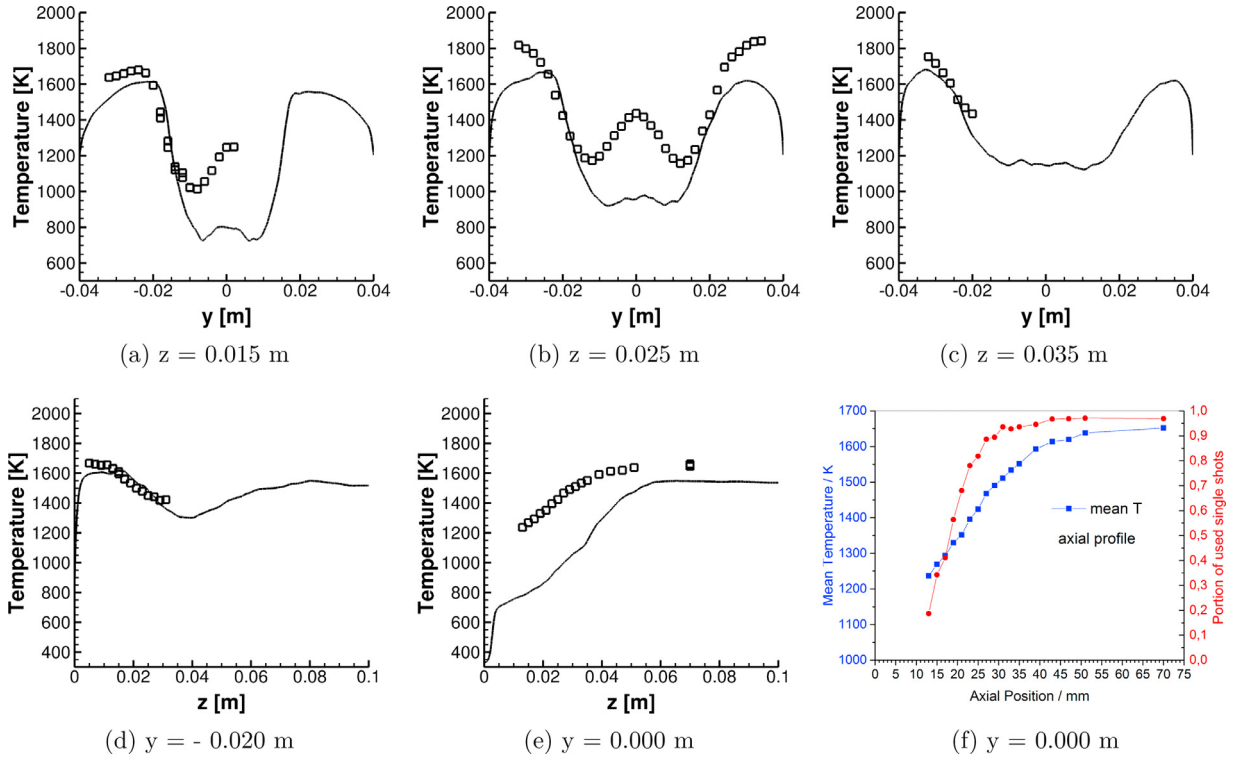

Fig. 17. Time-averaged horizontal (a–c) and vertical (d-e) temperature profiles at different positions: LES (black lines) and experimental data (black symbols), (f) Axial profile of the mean temperature measured by CARS (blue line) and portion of single-shot measurements used for the temperature determination (red line). (For interpretation of the references to color in this figure legend, the reader is referred to the web version of this article.)

(green symbols), and 50 µm (blue symbols), are plotted for the LES computation. In order to have a larger set of droplet data for the ensemble averages, a ±10% margin was introduced resulting in the following diameter ranges: 9 µm < d < 11 µm, 27 µm < d < 33 µm and 45 µm < d < 55 µm. From the PDA measurement, only the average velocity for all droplets is available. A one to one comparison is not possible, but from Fig. 16a it can be inferred that the measured profile reflects droplets in the size range 18 µm < d < 25 µm and 25 µm < d < 35 µm in the inner and outer region, respectively. Hence, in the outer range the measured velocities are comparable to the ones of the 30µm diameter class (green symbols). The axial and tangential velocity match well, while the radial velocity predicted by the LES is slightly lower. In the inner region, there is no corresponding diameter class but the values are expected to be between the ones for the 10 µm and 30 µm diameter class. This suggests that the radial and tangential velocity are well predicted by the LES while the axial velocity is slightly overpredicted.

4.8. Temperature profiles

Figure 17 shows a comparison of the time-averaged temperature profiles between the LES (lines) and experimental data (squares) from the CARS measurement system. Three horizontal profiles at z = 0.015 m, z = 0.025 m and z = 0.035 m (Fig. 17a–c) together with two vertical profiles at x = −0.02 m (Fig. 17c) and x = 0.0 m (Fig. 17e) are presented. The temperature rise at the beginning of the flame zone (zone 2) in the lower external recirculation zones is well reflected by the LES computation. In this region, the profiles match for all horizontal profiles (Fig. 17a–c). This is also confirmed by the vertical profile at y = −0.02 m (Fig. 17d). Although the temperatures at the confinements were measured, the cooling effect due to the isothermal walls seems to be overestimated in the computation resulting in a rapid temperature decay close to the confinements (see $|y| \geq 0.03$ in Fig. 17a–c and $z \leq 0.005$ in Fig. 17d). The experimentally observed maximum (time-averaged) temperature of 1820 K is therefore never reached in the entire simulation domain with a maximum (time-averaged) temperature in the LES of 1730 K. Furthermore, a clear discrepancy is observable in the central region, where the measurement shows another distinct temperature peak. A small peak is also visible in the simulation data but far less pronounced. This is also confirmed by the vertical profile along the z-axis (Fig. 17e). Although a similar temperature rise is visible in the LES data compared to the CARS data, a significant vertical offset of about 15–20 mm is evident. Furthermore, the final temperature level ($\sim$ 1660 K), which is reached for z > 0.05 m, is 100 K hotter than the one predicted by the LES. The discrepancies between measurement and computation might be due to differences in the temperature boundary conditions for the confinements mentioned above or the droplet starting conditions. For the latter, it was assumed that the entire spray issuing from the central pressure nozzle impinges on the pre-filmer surface and forms a film, which is finally atomized. However, it cannot be excluded that small droplets evaporate before hitting the surface. Furthermore, the flame temperatures were measured by single-shot coherent-anti-Stokes Raman spectroscopy (CARS) as described in [60]. In brief, for the measurements, three pulsed laser beams were overlapped in the measurement volume to generate the CARS signal beam by the interaction of the laser radiation with the non-linear susceptibility of the nitrogen molecules. The measurement volume had a diameter of approximately 0.1 mm and a length of 2.2 mm. When droplets were present in or nearby the probe volume, the high laser power densities could lead to an optical breakdown, i.e. ionization of molecules followed by a plasma generation. When optical breakdown occurred, the CARS signal was so heavily disturbed that a temperature evaluation was not possible. Such single-shot measurements were discarded. At each measurement location, typically 1200 single shot measurements were performed from which the temperature PDFs were

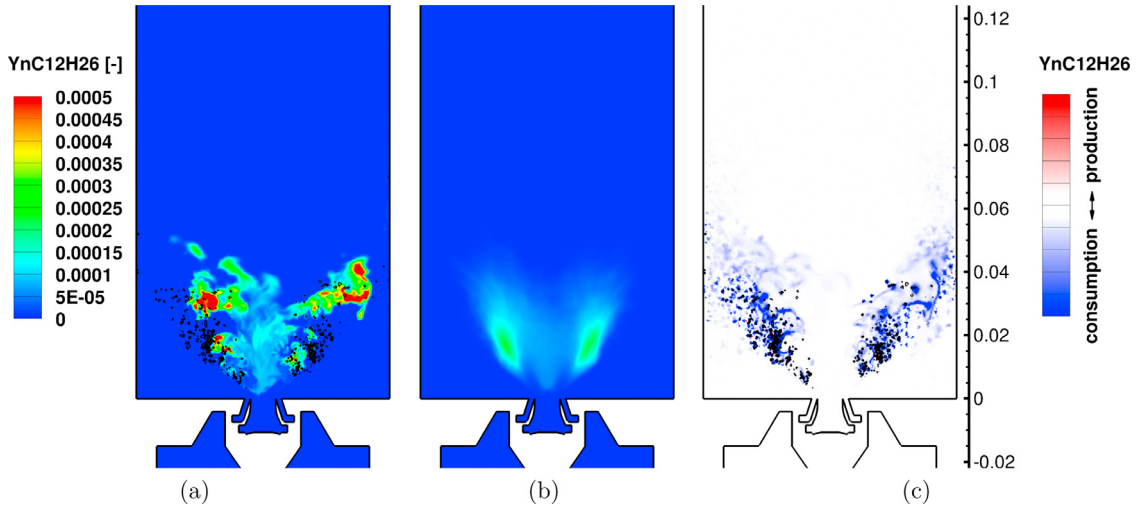

Fig. 18. Instantaneous (a) and time-averaged (b) gas concentration field as well as instantaneous net production / consumption rate (c) of n-dodecane. Black lines in the instantaneous snapshots show where n-dodecane evaporates.

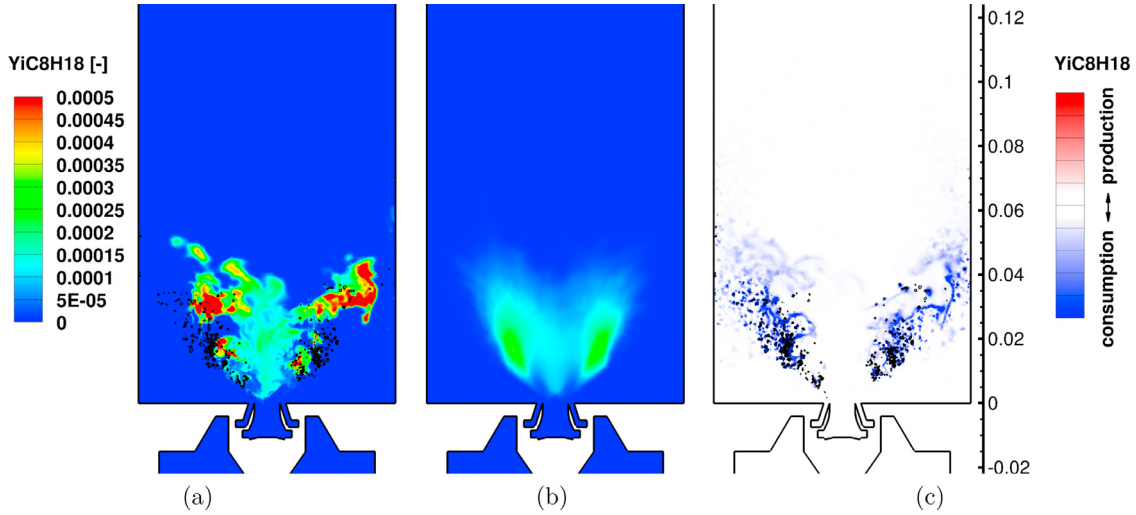

Fig. 19. Instantaneous (a) and time-averaged (b) gas concentration field as well as instantaneous net production / consumption rate (c) of iso-octane. Black lines in the instantaneous snapshots show where iso-octane evaporates.

set up. The discard of single-shot measurements is expected to bias the temperature PDF to higher temperatures because optical breakdown occurred predominantly in regions with high droplet loading and these regions were presumably rather cold. Although the bias cannot be quantified in the experiment, it must be kept in mind when comparing experimental and simulated temperature profiles. As an example, Fig. 17f displays the axial profile of the mean temperature together with the portion of used single shot CARS measurements from which the temperatures were deduced. Close to the nozzle, a large portion of measurements were discarded and the mean temperatures are certainly biased to a too high value. For positions with $z > 25$ mm the portion of used single shots is larger than 0.9 and a possible temperature bias is thus small. In order to clarify if the observed temperature differences are due this bias or are rather related to deficiencies in the boundary conditions, sub-models or reaction mechanism of the computation, further measurements and simulations will be necessary to analyze the sensitivity of the results on these aspects.

4.9. Vapor species fields, pollutant formation and emissions

Figures 18–21 show the instantaneous (a) and time-averaged gas concentrations of the fuel species as well as the instantaneous net production and consumption rate (c). The instantaneous snapshots (a and c) are overlaid with black lines illustrating where the fuel components evaporate. As expected, the only source of gaseous fuel species is through evaporation. The absence of gaseous fuel species around most of the evaporation locations (see Figs. 18a–21a) and the strong consumption in Figs. 18c–21c suggest that the evaporated fuel species immediately react in the flame zone (zone 2). In this zone, evaporation appears to be the rate controlling step, i.e. evaporation and mixing times introduce an inherent damping to combustion. In case the evaporated fuel species encounter a cold region in the incoming swirling air stream (zone 1) or the lower part of the upper mixing zone (zone 5), pockets of unburned gaseous fuel species can form (see Figs. 18a–21a). On average (Figs. 18b–21b), the maxima of the fuel species mass fractions are found in the shear layer between unmixed air stream (zone 1) and the flame zone (zone 2). The amount of species entrained into the lower central mixing zone (zone 4) is attributed to the evaporation and the chemical conversion rates of the individual species. The effect of different volatility can be seen for n-dodecane, iso-octane and cyclo-hexane (Figs. 18–20)), i.e., the faster the evaporation, the higher the mass fractions in the lower central recirculation zone. In Section 4.5, it is shown that the cyclo-alkanes evaporate before the iso-alkanes and

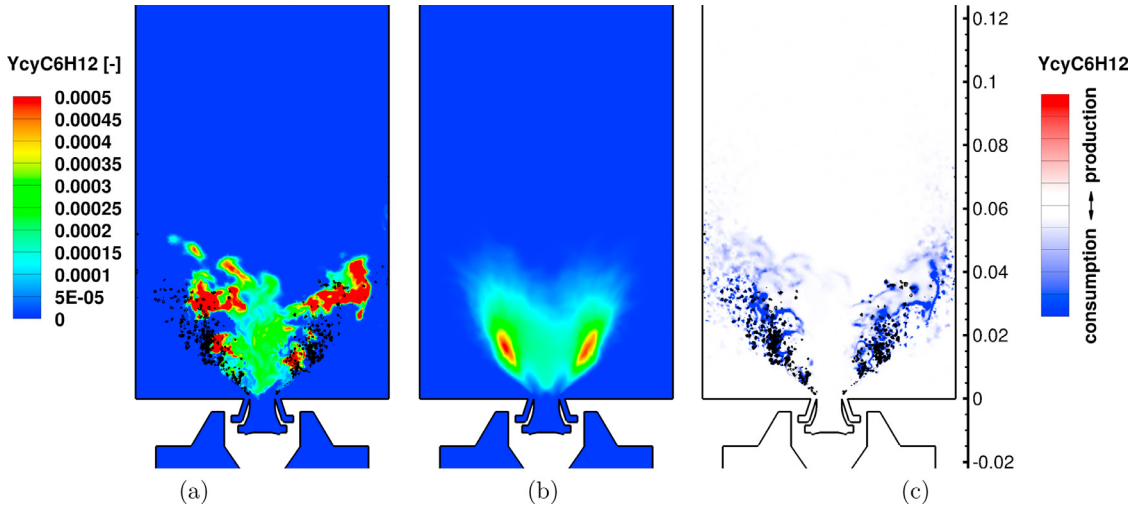

Fig. 20. Instantaneous (a) and time-averaged (b) gas concentration field as well as instantaneous net production / consumption rate (c) of cyclo-hexane. Black lines in the instantaneous snapshots show where cyclo-hexane evaporates.

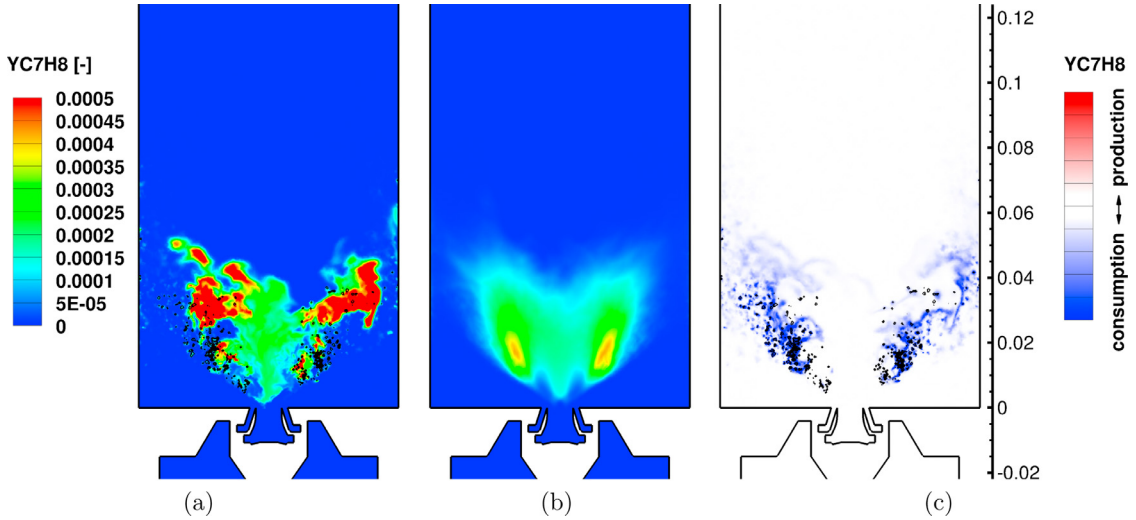

Fig. 21. Instantaneous (a) and time-averaged (b) gas concentration field as well as instantaneous net production / consumption rate (c) of toluene. Black lines in the instantaneous snapshots show where toluene evaporates.

the n-alkanes. The absolute values are also strongly related to the initial fuel composition of 22.49% n-alkanes, 20.82% iso-alkanes, 35.05% cyclo-alkanes and 21.64% aromatics. However, the toluene concentrations show that besides evaporation the chemical conversion rates of the individual fuel surrogate species effect the entrainment into the lower central mixing zone. Toluene exhibits a slow evaporation, but also the slowest chemical conversion rates of the four fuel surrogate species, which was observed in 1-d flames calculated with the same reaction mechanism (not shown here). As a consequence, toluene is present in the lower central recirculation zone, which has not yet reacted. Pollutant formation and emissions are not in the primary focus of this work, i.e. the detailed formation mechanisms for soot and NO_x were not considered. Nevertheless, the Zeldovich sub-mechanism for thermal NO formation from the GRI 3.0 reaction mechanism [36] and soot precursors such as benzene are included in the reaction mechanism (see Section 2.1.2). Figs. 22, 23 and 25 illustrate the instantaneous (a) and time-averaged gas concentrations of *NO, CO* and benzene as well as the instantaneous net production and consumption rate (c). As expected, *NO* forms in the high temperature region ($T > 1600$ K) (see Fig. 22) leading to the highest concentrations in the flame zone (zone 2). Nevertheless, the NO emissions of 1.3 ppm in the exhaust gas are not correctly predicted in the simulation being an order of magnitude lower than the measured value of 22.5 ppm. One reason for the discrepancy can be the underestimation of temperatures in the LES shown in Section 4.8. Besides, a closer look at the thermal NO sub-mechanism in the GRI 3.0 mechanism reveals that the constants differ from the ones given in the literature, e.g., in [61]. It is quite possible that the constants are only valid in conjunction with the other NO_x formation paths and the sub-mechanism should not be used isolated from these formation paths. According to Figs. 23 and 24, CO is mainly produced at the early stages of the fuel oxidation and then further oxidized to CO_2 in the presence of OH. In this manner, the major portion of CO is consumed but a small rest in the ppm-range is emitted. The CO emissions predicted by the LES amount to 20.3 ppm and are close to the 18.6 ppm experimentally determined in the exhaust gas. Although detailed predictions of soot emissions were not part of this study, the Jet A-1 reaction mechanism includes reaction paths, which lead to the formation of soot precursors, e.g., benzene (C_6H_6). The soot precursor benzene (Fig. 25) is mainly formed from toluene (C_7H_8) in regions where toluene is not directly oxidized, i.e., in locally toluene-rich discrete spots around the droplets and in regions occupied by toluene

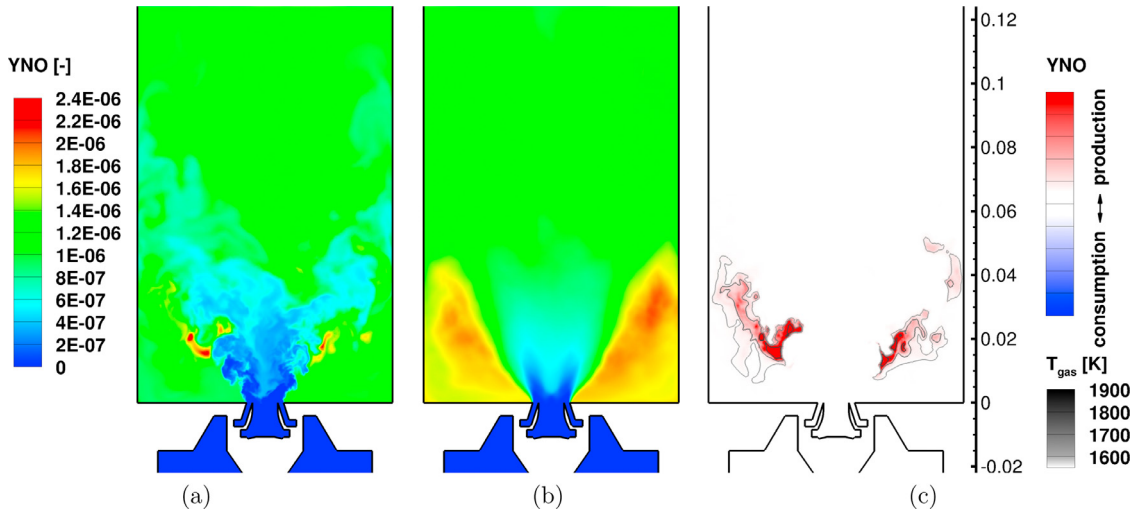

Fig. 22. Instantaneous (a) and time-averaged (b) gas concentration field as well as instantaneous net production / consumption rate (c) of nitrogen monoxide.

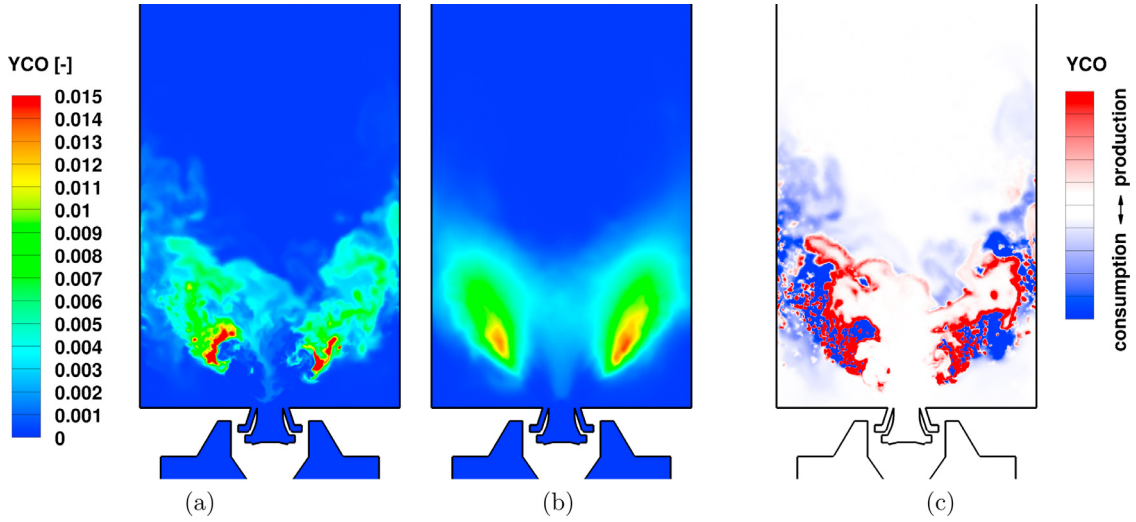

Fig. 23. Instantaneous (a) and time-averaged (b) gas concentration field as well as instantaneous net production / consumption rate (c) of carbon monoxide.

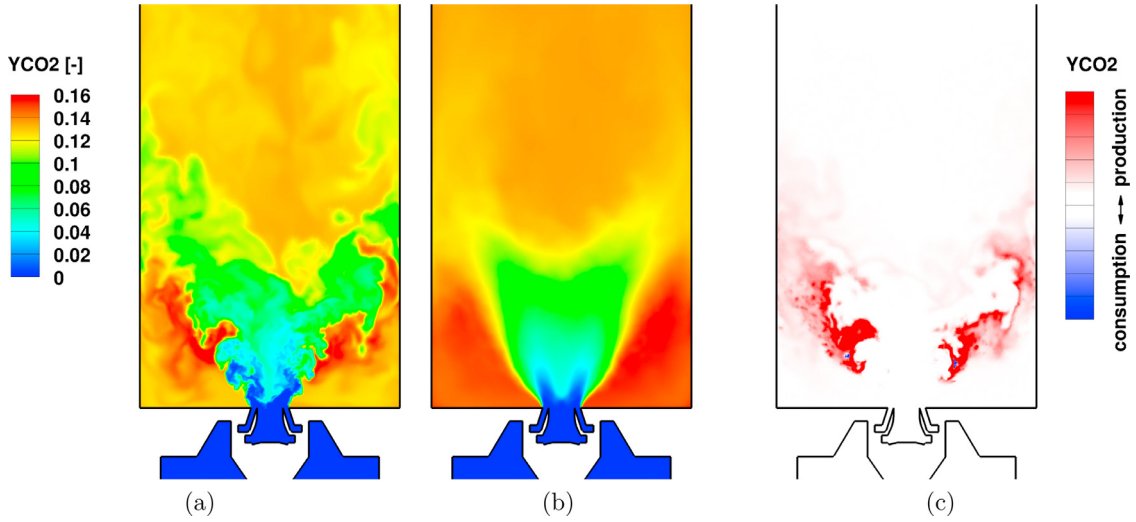

Fig. 24. Instantaneous (a) and time-averaged (b) gas concentration field as well as instantaneous net production / consumption rate (c) of carbon dioxide.

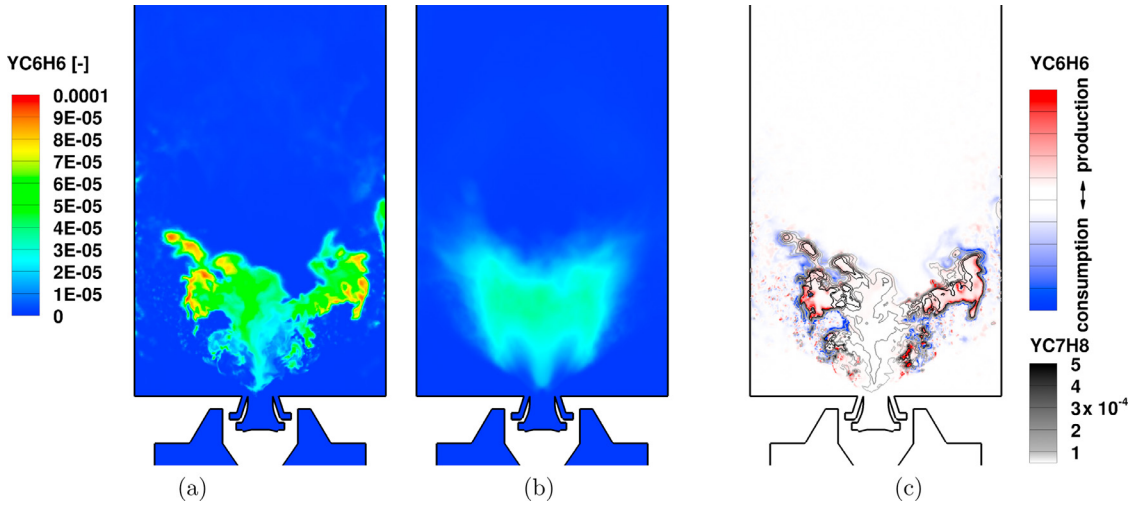

Fig. 25. Instantaneous (a) and time-averaged (b) gas concentration field as well as instantaneous net production / consumption rate (c) of benzene.

and temperatures $T < 1200$ K. It is consumed encountering regions with high temperatures. The example of benzene formation from one specific fuel family shows that a multi-component description of the liquid phase and the evaporation process is a necessary requirement for the prediction of soot emissions.

5. Conclusions

In the work at hand, the multi-component vaporization model of Tamim and Hallett [15,16] was coupled to a direct, detailed chemistry solver based on Arrhenius equations. The physical properties of the liquid were represented by the continuous thermodynamics approach in order to accurately describe the vaporization process while maintaining the computational costs at at reasonable level. The chemical surrogate for kerosene consisted of one representative species from the four most important chemical classes (n-alkanes, iso-alkanes, cyclo-alkanes and aromatics). By means of the computational platform, a lab-scale, swirl-stabilized spray burner was simulated. Exhibiting some of the key features of current aero-engines combustors, the test case has a high complexity. This is due to the fact that a multi-component fuel is introduced via a hybrid fuel injector with a complicated atomization pattern into a highly turbulent flow within a complex geometry. Furthermore, mixing and combustion take place with significant heat loss at the confinements. Accurate predictions of such complex systems are very challenging, especially as uncertainties concerning the boundary conditions for the confinements and the spray cannot be excluded. Despite these complications, global features like the measured spray distribution and the measured position of the reaction zone are well reproduced by the LES. The quantitative comparison of droplet size, droplet velocity and liquid volume flux profiles also show a good agreement. However, the temperature profiles reveal a significant discrepancy in the central mixing zone. In the LES, the temperature rise on the central axis is observed further towards the outlet. It could not be finally clarified if the discrepancies are related to a bias in the measurement, differences in boundary conditions or still existing deficiencies in the submodels. Further simulations and measurements will be necessary to analyze the sensitivity of the results on these aspects. Especially the proper representation of the atomization process in combustion simulations is still a major scientific challenge and involves high uncertainties. Universally valid, accurate and efficient models, which can be embedded into simulation tools, are yet not available and need to be in the focus of future research programs. Nevertheless, the analysis presented in Section 4 show the great potential of spray combustion LES. In comparison to measurements, a large set of simultaneously taken three-dimensional data with a high temporal and spatial resolution is available. Therefore, LES can help in the understanding and interpretation of complex phenomena. In this context, the simulations showed that evaporation and mixing are the rate-controlling steps in the flame zone. In this zone, chemistry can be assumed to be infinitely fast. That means that evaporation and mixing times introduce an inherent damping to combustion. These findings directly relate to modern combustion concepts explaining why the trend towards a higher degree of prevaporization and premixing makes these combustion systems more susceptible to instabilities. In contrast to the infinitely fast chemistry in the flame zone, other zones exist where finite rate chemistry effects prevail. For these states, the direct computation of the elementary reactions by means of Arrhenius equations and the transport of all individual species are beneficial. Furthermore, the finite rate chemistry approach demonstrates a great potential with respect to pollutant formation, as precursors can be directly computed. The example of benzene forming from one specific chemical class in the fuel additionally shows that a multi-component description of the liquid phase and the evaporation process is required to correctly predict soot emissions.

Acknowledgment

The research leading to these results has received funding from the DLR internal project ECLIF (Emissions and CLimate Impact of alternative Fuels). Futhermore, the authors gratefully acknowledge the Gauss Centre for Supercomputing e.V. (GCS, www.gauss-centre.eu) for funding this project by providing computing time on the GCS supercomputer SuperMUC at Leibniz Supercomputing Centre (LRZ, www.lrz.de).

References

[1] F.L. Dryer, Chemical kinetic and combustion characteristics of transportation fuels, Proc. Combust. Inst. 35 (1) (2015) 117–144, doi:10.1016/j.proci.2014.09.008.
[2] M. Braun-Unkhoff, T. Kathrotia, B. Rauch, U. Riedel, About the interaction between composition and performance of alternative jet fuels, CEAS Aeronaut. J. 7 (1) (2016) 83–94, doi:10.1007/s13272-015-0178-8.
[3] M. Braun-Unkhoff, U. Riedel, C. Wahl, About the emissions of alternative jet fuels, CEAS Aeronaut. J. 8 (1) (2017) 167–180, doi:10.1007/s13272-016-0230-3.
[4] M. Colket, J. Heyne, M. Rumizen, M. Gupta, T. Edwards, W.M. Roquemore, G. Andac, R. Boehm, J. Lovett, R. Williams, J. Condevaux, D. Turner, N. Rizk, J. Tishkoff, C. Li, J. Moder, D. Friend, V. Sankaran, Overview of the national jet fuels combustion program, AIAA J. 55 (4) (2017), doi:10.2514/1.J055361.
[5] C. Wahl, M. Kapernaum, Report on kerosene validation data, final report, DLR - German Aerospace Center, 2003. G4RD-CT-00075.

[6] P. Dagaut, M. Cathonnet, The ignition, oxidation, and combustion of kerosene: a review of experimental and kinetic modeling, Prog. Energy Combust. Sci. 32 (1) (2006) 48–92, doi:10.1016/j.pecs.2005.10.003.

[7] M. Rachner, M. Brandt, H. Eickhoff, C. Hassa, A. Bräumer, H. Krämer, M. Ridder, V. Sick, A numerical and experimental study of fuel evaporation and mixing for lean premixed combustion at high pressure, Symp. (Int.) Combust. 26 (2) (1996) 2741–2748, doi:10.1016/S0082-0784(96)80111-1.

[8] M. Rachner, Die Stoffeigenschaften von Kerosin Jet A-1, DLR-Mitteilung, DLR - German Aerospace Center, 1998. 98-01.

[9] W. Jones, S. Lyra, S. Navarro-Martinez, Numerical investigation of swirling kerosene spray flames using large eddy simulation, Combust. Flame 159 (4) (2012) 1539–1561, doi:10.1016/j.combustflame.2011.10.025.

[10] T. Edwards, L.Q. Maurice, Surrogate mixtures to represent complex aviation and rocket fuels, J. Propuls. Power 17 (2) (2001) 461–466, doi:10.2514/2.5765.

[11] L. Shafer, R. Striebich, J. Gomach, T. Edwards, Chemical class composition of commercial jet fuels and other specialty kerosene fuels, 14th AIAA/AHI Space Planes and Hypersonic Systems and Technologies Conference (2006), doi:10.2514/6.2006-7972.

[12] A. Violi, S. Yan, E.G. Eddings, A.F. Sarofim, S. Granata, T. Faravelli, E. Ranzi, Experimental formulation and kinetic model for JP-8 surrogate mixtures, Combust. Sci. Technol. 174 (11–12) (2002) 399–417, doi:10.1080/00102200215080.

[13] D. Kim, J. Martz, A. Violi, A surrogate for emulating the physical and chemical properties of conventional jet fuel, Combust. Flame 161 (6) (2014) 1489–1498, doi:10.1016/j.combustflame.2013.12.015.

[14] D. Kim, J. Martz, A. Abdul-Nour, X. Yu, M. Jansons, A. Violi, A six-component surrogate for emulating the physical and chemical characteristics of conventional and alternative jet fuels and their blends, Combust. Flame 179 (2017) 86–94, doi:10.1016/j.combustflame.2017.01.025.

[15] J. Tamim, W. Hallett, A continuous thermodynamics model for multicomponent droplet vaporization, Chem. Eng. Sci. 50 (18) (1995) 2933–2942, doi:10.1016/0009-2509(95)00131-N.

[16] W.L. Hallett, A simple model for the vaporization of droplets with large numbers of components, Combust. Flame 121 (1–2) (2000) 334–344, doi:10.1016/S0010-2180(99)00144-3.

[17] P.C. Le Clercq, J. Bellan, Direct numerical simulation of a transitional temporal mixing layer laden with multicomponent-fuel evaporating drops using continuous thermodynamics, Phys. Fluids (1994-present) 16 (6) (2004) 1884–1907, doi:10.1063/1.1688327.

[18] P.C. Le Clercq, J. Bellan, Direct numerical simulation of gaseous mixing layers laden with multicomponent-liquid drops: liquid-specific effects, J. Fluid Mech. 533 (2005) 57–94, doi:10.1017/S0022112005003940.

[19] B. Franzelli, B. Fiorina, N. Darabiha, A tabulated chemistry method for spray combustion, Proc. Combust. Inst. 34 (1) (2013) 1659–1666, doi:10.1016/j.proci.2012.06.013.

[20] H. Olguin, E. Gutheil, Influence of evaporation on spray flamelet structures, Combust. Flame 161 (4) (2014) 987–996, doi:10.1016/j.combustflame.2013.10.010.

[21] N. Slavinskaya, E. Saibov, U. Riedel, J. Herzler, C. Naumann, L. Thomas, M. Saffaripour, Kinetic surrogate model for GTL kerosene, AIAA SciTech 2014 - 52nd Aerospace Sciences Meeting, American Institute of Aeronautics and Astronautics (2014), doi:10.2514/6.2014-0126.

[22] S.H. Won, F.M. Haas, S. Dooley, T. Edwards, F.L. Dryer, Reconstruction of chemical structure of real fuel by surrogate formulation based upon combustion property targets, Combust. Flame 183 (2017) 39–49, doi:10.1016/j.combustflame.2017.04.032.

[23] H. Wang, R. Xu, K. Wang, C.T. Bowman, R.K. Hanson, D.F. Davidson, K. Brezinsky, F.N. Egolfopoulos, A physics-based approach to modeling real-fuel combustion chemistry – I. Evidence from experiments, and thermodynamic, chemical kinetic and statistical considerations, Combust. Flame 193 (2018) 502–519, doi:10.1016/j.combustflame.2018.03.019.

[24] G. Eckel, J. Grohmann, M. Rachner, P. Le Clercq, M. Aigner, Les of a generic swirl-stabilized spray burner with detailed chemistry, 9th U.S. National Combustion Meeting,1B17, Cincinnati, Ohio, USA (2015).

[25] B. Franzelli, A. Vié, M. Boileau, B. Fiorina, N. Darabiha, Large eddy simulation of swirled spray flame using detailed and tabulated chemical descriptions, Flow, Turbul. Combust. 98 (2) (2017) 633–661, doi:10.1007/s10494-016-9763-0.

[26] A. Felden, L. Esclapez, E. Riber, B. Cuenot, H. Wang, Including real fuel chemistry in LES of turbulent spray combustion, Combust. Flame 193 (2018) 397–416, doi:10.1016/j.combustflame.2018.03.027.

[27] A. Panchal, R. Ranjan, S. Menon, Effect of chemistry modeling on flame stabilization of a swirl spray combustor, Joint Propulsion Conference, AIAA Propulsion and Energy Forum (2018), doi:10.2514/6.2018-4684.

[28] V.R. Hasti, P. Kundu, G. Kumar, S.A. Drennan, S. Som, S.H. Won, F.L. Dryer, J.P. Gore, Lean blow-out (LBO) computations in a gas turbine combustor, Joint Propulsion Conference, AIAA Propulsion and Energy Forum, Cincinnati, Ohio, USA (2018), doi:10.2514/6.2018-4958.

[29] G. Faeth, Evaporation and combustion of sprays, Prog. Energy Combust. Sci. 9 (1) (1983) 1–76, doi:10.1016/0360-1285(83)90005-9.

[30] J. Löwe, A. Probst, T. Knopp, R. Kessler, A low-dissipation low-dispersion second-order scheme for unstructured finite-volume flow solvers, 53rd AIAA Aerospace Sciences Meeting (2015). Kissimmee, Florida.

[31] F. Ducros, F. Nicoud, T. Poinsot, A wall-adapting local eddy-viscosity model for simulations in complex geometries, Conference on Numerical Methods for Fluid Dynamics (1998). Oxford, UK.

[32] F. Nicoud, F. Ducros, Subgrid-scale stress modelling based on the square of the velocity gradient tensor, Flow, Turbul. Combust. 62 (3) (1999) 183–200, doi:10.1023/A:1009995426001.

[33] K.K. Kuo, Principles of combustion, Wiley, New York, 1986.

[34] M. Di Domenico, Numerical simulations of soot formation in turbulent flows, Ph.D. thesis, Fakultät für Luft- und Raumfahrttechnik und Geodäsie, Universität Stuttgart, 2008.

[35] N. Slavinskaya, M. Abbasi, T. Kathrotia, U. Riedel, Reduced mechanism for kerosene combustion, 2015, (private communication).

[36] G.P. Smith, D.M. Golden, M. Frenklach, N.W. Moriarty, B. Eiteneer, M. Goldenberg, C.T. Bowman, R.K. Hanson, S. Song, W.C. Gardiner Jr., V.V. Lissianski, Z. Qin, Gri 3.0 mech (2000).

[37] T. Kathrotia, Reaction kinetics modeling of OH*, CH*, and C2* chemiluminescence, Ph.D. thesis, Ruprecht-Karls-Universität Heidelberg, 2011.

[38] M. Bini, W.P. Jones, Large-eddy simulation of particle-laden turbulent flows, J. Fluid Mech. 614 (2008) 207–252, doi:10.1017/S0022112008003443.

[39] G. Eckel, P. Le Clercq, T. Kathrotia, A. Saenger, S. Fleck, M. Mancini, T. Kolb, M. Aigner, Entrained flow gasification. part 3: insight into the injector near-field by large eddy simulation with detailed chemistry, Fuel 223 (2018) 164–178, doi:10.1016/j.fuel.2018.02.176.

[40] F. Tanner, Development and validation of a cascade atomization and drop breakup model for high-velocity dense sprays, At. Sprays 14 (2004) 211–242.

[41] R. Schmehl, Tropfendeformation und Nachzerfall bei der technischen Gemischaufbereitung, Ph.D. thesis, Universität Karlsruhe, 2004.

[42] R. Clift, J.R. Grace, M.E. Weber, Bubbles, drops, and particles, Academic Press New York, 1978.

[43] B. Abramzon, W. Sirignano, Droplet vaporization model for spray combustion calculations, Int. J. Heat Mass Transf. 32 (9) (1989) 1605–1618.

[44] N. Doué, P. Le Clercq, M. Aigner, Validation of a multicomponent-fuel droplet evaporation model based on continuous thermodynamics, ICLASS 2006 - 10th International Conference on Liquid Atomization and Spray Systems (2006).

[45] C.H. Whitson, Characterizing hydrocarbon plus fractions, Soc. Pet. Eng. J. 23 (04) (1983), doi:10.2118/12233-PA.

[46] N. Doué, P. Le Clercq, M. Aigner, A new multicomponent-fuel droplet vaporization model based on continuous thermodynamics theory using fourier series, 3rd European Combustion Meeting (2007). Chania, Greece.

[47] P. Le Clercq, N. Doué, M. Rachner, M. Aigner, Validation of a multicomponent–fuel model for spray computations, 47th AIAA Aerospace Sciences Meeting and Exhibit (2009). AIAA 2009-1188.

[48] G. Eckel, Large Eddy simulation of turbulent reacting multi-phase flows, Ph.D. thesis, Faculty of Aerospace Engineering and Geodesy of the University of Stuttgart, 2018.

[49] J. Grohmann, W. O'Loughlin, W. Meier, M. Aigner, Comparison of the combustion characteristics of liquid single-component fuels in a gas turbine model combustor, ASME Turbo Expo 2016: Power for Land, Sea, and Air, GT2016-56177 (2016).

[50] J. Grohmann, B. Rauch, T. Kathrotia, W. Meier, M. Aigner, Influence of single-component fuels on gas-turbine model combustor lean blowout, J. Propuls. Power 34 (1) (2018) 97–107, doi:10.2514/1.B36456.

[51] P. Nau, Z. Yin, O. Lammel, W. Meier, Wall temperature measurements in gas turbine combustors with thermographic phosphors, J. Eng. Gas Turbines Power (2018) 041021–041029 Article no. 0742–4795, doi:10.1115/1.4040716.

[52] C. Tropea, Optical particle characterization in flows, Ann. Rev. Fluid Mech. 43 (1) (2011) 399–426, doi:10.1146/annurev-fluid-122109-160721.

[53] N. Syred, A review of oscillation mechanisms and the role of the precessing vortex core (PVC) in swirl combustion systems, Prog. Energy Combust. Sci. 32 (2) (2006) 93–161, doi:10.1016/j.pecs.2005.10.002.

[54] R. Bilger, S. Stårner, R. Kee, On reduced mechanisms for methane-air combustion in nonpremixed flames, Combust. Flame 80 (2) (1990) 135–149, doi:10.1016/0010-2180(90)90122-8.

[55] T. Kathrotia, U. Riedel, A. Seipel, K. Moshammer, A. Brockhinke, Experimental and numerical study of chemiluminescent species in low-pressure flames, Appl. Phys. B 107 (3) (2012) 571–584, doi:10.1007/s00340-012-5002-0.

[56] B. Prabasena, M. Röder, T. Kathrotia, U. Riedel, T. Dreier, C. Schulz, Strain rate and fuel composition dependence of chemiluminescent species profiles in non-premixed counterflow flames: comparison with model results, Appl. Phys. B 107 (3) (2012) 561–569, doi:10.1007/s00340-012-4989-6.

[57] H. Yamashita, M. Shimada, T. Takeno, A numerical study on flame stability at the transition point of jet diffusion flames, Symp. (Int.) Combust. 26 (1) (1996) 27–34, doi:10.1016/S0082-0784(96)80196-2.

[58] N. Patel, S. Menon, Simulation of spray-turbulence-flame interactions in a lean direct injection combustor, Combust. Flame 153 (1?2) (2008) 228–257, doi:10.1016/j.combustflame.2007.09.011.

[59] D.G. Goodwin, H.K. Moffat, R.L. Speth, Cantera: an object-oriented software toolkit for chemical kinetics, thermodynamics, and transport processes, 2017, (http://www.cantera.org). Version 2.3.0.

[60] L.M. Cantu, J. Grohmann, W. Meier, M. Aigner, Temperature measurements in confined swirling spray flames by vibrational coherent anti-stokes raman spectroscopy, Expe. Therm. Fluid Sci. 95 (2018) 52–59. Tenth Mediterranean Combustion Symposium, doi: 10.1016/j.expthermflusci.2018.01.029.

[61] J. Warnatz, U. Maas, R. Dibble, Combustion – physical and chemical fundamentals, modeling and simulation, experiments, pollutant formation, 4 ed., Springer, Berlin Heidelberg, 2006.